JCI insight

RESEARCH ARTICLE

Gigaxonin glycosylation regulates intermediate filament turnover and may impact giant axonal neuropathy etiology or treatment

Po-Han Chen,[1,2,3] Jimin Hu,[1] Jianli Wu,[2,3] Duc T. Huynh,[1] Timothy J. Smith,[1] Samuel Pan,[2,3] Brittany J. Bisnett,[1] Alexander B. Smith,[2,3] Annie Lu,[2,3] Brett M. Condon,[1] Jen-Tsan Chi,[2,3] and Michael Boyce[1]

[1]Department of Biochemistry, [2]Department of Molecular Genetics and Microbiology, and [3]Center for Genomic and Computational Biology, Duke University School of Medicine, Durham, North Carolina, USA.

Gigaxonin (also known as KLHL16) is an E3 ligase adaptor protein that promotes the ubiquitination and degradation of intermediate filament (IF) proteins. Mutations in human gigaxonin cause the fatal neurodegenerative disease giant axonal neuropathy (GAN), in which IF proteins accumulate and aggregate in axons throughout the nervous system, impairing neuronal function and viability. Despite this pathophysiological significance, the upstream regulation and downstream effects of normal and aberrant gigaxonin function remain incompletely understood. Here, we report that gigaxonin is modified by *O*-linked β-*N*-acetylglucosamine (O-GlcNAc), a prevalent form of intracellular glycosylation, in a nutrient- and growth factor–dependent manner. MS analyses of human gigaxonin revealed 9 candidate sites of O-GlcNAcylation, 2 of which — serine 272 and threonine 277 — are required for its ability to mediate IF turnover in gigaxonin-deficient human cell models that we created. Taken together, the results suggest that nutrient-responsive gigaxonin O-GlcNAcylation forms a regulatory link between metabolism and IF proteostasis. Our work may have significant implications for understanding the nongenetic modifiers of GAN phenotypes and for the optimization of gene therapy for this disease.

Introduction

Giant axonal neuropathy. Giant axonal neuropathy (GAN) is a rare neurodegenerative disease characterized by abnormally large and dysfunctional axons (1). GAN first manifests as severe peripheral motor and sensory neuropathy during infancy and later evolves into central nervous system pathology, including seizures and cognitive impairment (2–4). Most individuals with GAN become nonambulatory early in the first decade of life and eventually develop widespread polyneuropathy and dementia (1, 5). Death usually occurs from respiratory failure by age 40 years (1, 5).

GAN is caused by loss-of-function mutations in the *GAN* gene, which encodes the gigaxonin protein (2). Gigaxonin (also known as KLHL16) belongs to the Kelch-like (KLHL) protein family, which typically contains broad complex/tramtrack/bric-a-brac (BTB), BTB and C-terminal Kelch (BACK), and Kelch domains (6). Structural and functional studies in representative KLHL family members have demonstrated that the BTB domain interacts with cullin 3 (CUL3), a component of E3 ubiquitin ligase complexes, while the KLHL Kelch domains recruit substrates for polyubiquitination (7). Therefore, KLHL proteins are generally considered to be adaptors for CUL3-containing E3 ligase complexes, regulating the ubiquitination and, usually, proteolysis of specific substrates.

Gigaxonin promotes the ubiquitination and turnover of IFs, and defective gigaxonin in GAN patients causes neurofilament-L (NF-L) and other IF proteins to accumulate in the axons of neurons (2, 8, 9). Interestingly, this function of gigaxonin is not restricted to the nervous system. For example, gigaxonin is required for the normal proteolysis of vimentin and keratins in fibroblasts, and GAN patients often exhibit curly hair due to high keratin levels (10, 11). Disease-causing *GAN* mutations disable gigaxonin by several mechanisms, including reducing the abundance of its mRNA, destabilizing the protein, and/or impairing

Conflict of interest: The authors have declared that no conflict of interest exists.

Submitted: January 27, 2019
Accepted: November 21, 2019
Published: January 16, 2020.

Reference information: *JCI Insight*. 2020;5(1):e127751. https://doi.org/10.1172/jci.insight.127751.

its biochemical activity (9). Reciprocally, experimental reexpression of gigaxonin in WT or *GAN*-deficient cells results in the clearance of accumulated IFs (12).

While the regulation and function of gigaxonin remain incompletely understood, several lines of evidence suggest possible connections to cell metabolism. For example, *GAN*-deficient cells exhibit dysregulated mitochondrial distribution and behavior (10, 13). In *GAN* loss-of-function cells, mitochondria often colocalize with ovoid IF aggregates, frequently found near the nucleus, and mitochondrial motility is reduced (10, 13). Although mitochondrial inner membrane potential is not affected by loss of gigaxonin function (13), the oxygen consumption rate is increased in *GAN*-knockout, *GAN*-knockdown, and *CUL3*-knockdown cells (10), consistent with functional links among gigaxonin/CUL3 complexes, IFs, and mitochondrial physiology. Furthermore, while ovoid IF aggregates are observed in 3%–15% of *GAN*-deficient cells grown under standard culture conditions, this phenotype is significantly exacerbated (to 48%–88%) by serum starvation (8), indicating that nutrient or growth factor signaling affects gigaxonin function. Therefore, the severity of GAN phenotypes may be modulated by nongenetic factors such as metabolic status. Together, these observations suggest that nutrient cues affect the activity of gigaxonin and its regulation of the IF cytoskeleton, but the underlying mechanisms remain unknown.

O-GlcNAcylation and the KLHL family. In previous work, we discovered a novel connection between the KLHL protein family and O-GlcNAcylation (14). *O*-linked β-*N*-acetylglucosamine (O-GlcNAc) is an abundant form of intracellular glycosylation that reversibly decorates serines and threonines of thousands of nuclear, cytoplasmic, and mitochondrial proteins (15, 16). In mammals, O-GlcNAc is added by O-GlcNAc transferase (OGT) and removed by O-GlcNAcase (OGA) in response to a wide range of physiological signals (15–18). UDP-GlcNAc, the nucleotide-sugar cofactor used by OGT, is created by the hexosamine biosynthetic pathway (HBP) from multiple essential metabolites, including glucose, glutamine, acetyl–coenzyme A, uridine, and ATP (19–22). Therefore, fluctuations in these nutrients or growth factors affect the levels of both UDP-GlcNAc and O-GlcNAc, making the modification a sentinel of cell metabolism (16, 22–30). O-GlcNAc cycling controls myriad processes, including cell metabolism, cell cycle progression, and cell death (15, 16, 18), and is essential, as genetic ablation of OGT or OGA in mice is lethal (31–33). Aberrant O-GlcNAcylation is also implicated in numerous human diseases, including various forms of neurodegeneration, further underscoring its functional importance (22, 34–42).

Recently, we reported that the KLHL family member KEAP1 (also known as KLHL19) is O-GlcNAcylated. Specific O-GlcNAc sites are necessary for the ability of KEAP1 to mediate the ubiquitination and destruction of NRF2, its best-known target and a master transcriptional regulator of redox stress responses (14, 43, 44). Due to the structural and functional similarities among the KLHL proteins, we speculated that other family members may also be O-GlcNAcylated. Indeed, a pilot experiment suggested that gigaxonin is a potential O-GlcNAc substrate (14). Here, we report that gigaxonin is O-GlcNAcylated on up to 9 specific residues in a nutrient-responsive manner. Using human gigaxonin loss-of-function neuroblastoma and fibroblast model systems that we created, we identified 2 specific gigaxonin O-GlcNAc sites that are required for its ability to interact with IF proteins and to promote their turnover. Our results provide molecular insight into the potential metabolic regulation of the IF cytoskeleton through gigaxonin O-GlcNAcylation and may inform our understanding of GAN disease modifiers and the optimization of GAN gene therapy.

Results

Mass spectrometry identifies candidate O-GlcNAc sites on gigaxonin. In a previous study focused on KEAP1 glycosylation (14), we discovered initial evidence of gigaxonin modification by O-GlcNAc. We hypothesized that gigaxonin O-GlcNAcylation might regulate its function in IF protein turnover, analogous to the role of KEAP1 O-GlcNAcylation in governing the ubiquitination and stabilization of its target NRF2 (14). To test this hypothesis, we first confirmed the O-GlcNAcylation of endogenous gigaxonin in a variety of cell types. In SH-SY5Y neuroblastoma cells, gigaxonin was dynamically modified by O-GlcNAc, as the degree of glycosylation was reduced by treatment with a small molecule inhibitor of OGT ($Ac_4$5SGlcNAc, or 5SG) and enhanced by a small molecule inhibitor of OGA (Thiamet G) (Figure 1A). Because gigaxonin regulates IF proteins in nonneuronal tissues as well (45–47), we asked whether these observations extended to other cell types. Indeed, we observed dynamic gigaxonin O-GlcNAcylation in both HeLa (Figure 1B) and MDA-MB-231 cells (Figure 1C), supporting gigaxonin O-GlcNAcylation as a broad phenomenon across disparate cell types.

To identify O-GlcNAcylated residues on gigaxonin, we expressed myc-6xHis–tagged gigaxonin in HEK293T (293T) cells, a facile human expression system, and obtained highly purified protein via tandem IP

using anti-myc antibody and immobilized metal affinity chromatography (Figure 1D). Purified gigaxonin from 2 biological replicates was digested in-gel and analyzed by mass spectrometry (MS) to identify O-GlcNAc sites.

In our first MS experiment, we identified 9 candidate O-GlcNAc sites on gigaxonin. Five sites (T207, S219, S224, S228, and S229) resided in the BACK domain, which was recently reported to be required for interaction with the autophagy protein ATG16L1 (48). Three other sites (S249, S254, S272) lay in the junction between the BACK and the first Kelch domains, and the last site (T277) was within the first Kelch domain, which was predicted to interact with gigaxonin's ubiquitination substrates (49) (Figure 1E and Supplemental Figure 1A; supplemental material available online with this article; https://doi.org/10.1172/jci.insight.127751DS1). In a second MS analysis of an independently expressed and purified gigaxonin sample, we again observed the glycosylation of S228, S229, S272, and T277, underlining the reproducibility of the methodology and providing strong evidence for the O-GlcNAcylation of these residues.

To identify the major in vivo O-GlcNAcylation site(s) on gigaxonin, we expressed WT or unglycosylatable (Ser/Thr→Ala) point mutant constructs in 293T cells and analyzed them by IP/Western blotting (WB). No single point mutation dramatically reduced total detectable gigaxonin O-GlcNAcylation under standard culture conditions, possibly due to the simultaneous modification of multiple sites or to technical limitations of the available anti–O-GlcNAc antibodies (data not shown). On the other hand, upon inhibition of OGA by Thiamet G, the S272A and T277A mutants, when compared with WT, showed modestly impaired increases in O-GlcNAc signal (Supplemental Figure 1B). This result suggests that inducible gigaxonin O-GlcNAcylation may occur primarily at S272 and/or T277.

Gigaxonin loss-of-function neuroblastoma and fibroblast cells provide GAN model systems. Primary fibroblasts from GAN patients have been powerful tools for dissecting the functional impact of gigaxonin mutants, but they are genetically heterogeneous and often exhibit variable IF phenotypes (e.g., 3%–15% of cells displaying ovoid aggregates), which may confound the interpretation of some experiments (8, 50). Mouse models of GAN have also been valuable but exhibit less-severe neurodegeneration than do humans, suggesting potentially important species-dependent differences (51–53). Therefore, we used CRISPR genome engineering to ablate endogenous gigaxonin expression in human cells, establishing *GAN*$^{-/-}$ systems that reliably recapitulate cellular GAN disease phenotypes and permit functional tests of gigaxonin mutants. We envision that such tractable human cell lines would provide a useful complement to existing GAN primary cell and mouse systems. We chose SH-SY5Y and BJ5ta (immortalized human fibroblast) cells as appropriate models based on previous reports of gigaxonin function and IF protein accumulation in these cell types (12). Multiple guide RNAs (gRNAs) targeting *GAN* exon 1 were designed and subcloned into a lentiCRISPR vector (54). After selection, *GAN*$^{-/-}$ SH-SY5Y cells exhibited reduced proliferation, and many grew as individual cells rather than in the clusters seen in the parental cell line (Supplemental Figure 2A).

To confirm successful *GAN* deletion, we evaluated gigaxonin and vimentin expression in *GAN*$^{-/-}$ cells by WB and quantitative PCR (qPCR). Gigaxonin protein and mRNA were depleted in the *GAN*-targeted cells (Figure 2, A and B), with a corresponding dramatic increase in endogenous vimentin protein (Figure 2A and Supplemental Figure 2B). By immunofluorescence assay (IFA), most *GAN*$^{-/-}$ SH-SY5Y (Figure 2C) and BJ5ta (Supplemental Figure 2C) cells showed single, perinuclear, and ovoid vimentin aggregates, similar to previously reported phenotypes in primary cells from GAN patients (Figure 2C) (8, 12). Quantification of distinct *GAN*$^{-/-}$ cell lines generated with different sgRNAs showed that greater than 80% of cells (sgRNAs 1 and 3) contained perinuclear ovoid aggregates (Figure 2D). Aggregates colocalized with the microtubule organizing center but not with Golgi markers (Figure 3, A and B). Consistent with a previous report (8), F-actin distribution was not affected by gigaxonin loss (Figure 3C), demonstrating the specific effect of *GAN* deletion on the IF compartment. In addition, we also observed aggregation and colocalization of NF-L with vimentin in *GAN*$^{-/-}$ SH-SY5Y cells (Figure 3D).

To further confirm our CRISPR results by an independent method, we established stable shRNA-mediated *GAN*-knockdown (shGAN) cell lines. As expected, we observed vimentin increases and aggregation in shGAN SH-SY5Y cells using both WB (Supplemental Figure 2D) and IFA (Supplemental Figure 2E). Importantly, shGAN cells showed cellular morphology similar to that of *GAN*$^{-/-}$ cells, and reexpression of WT shRNA-resistant gigaxonin abolished both the vimentin accumulation (Supplemental Figure 2, D–F) and the cellular morphology phenotypes (Supplemental Figure 2G). Rescue of these GAN-like phenotypes by gigaxonin reexpression confirmed the specificity and validity of our cell systems.

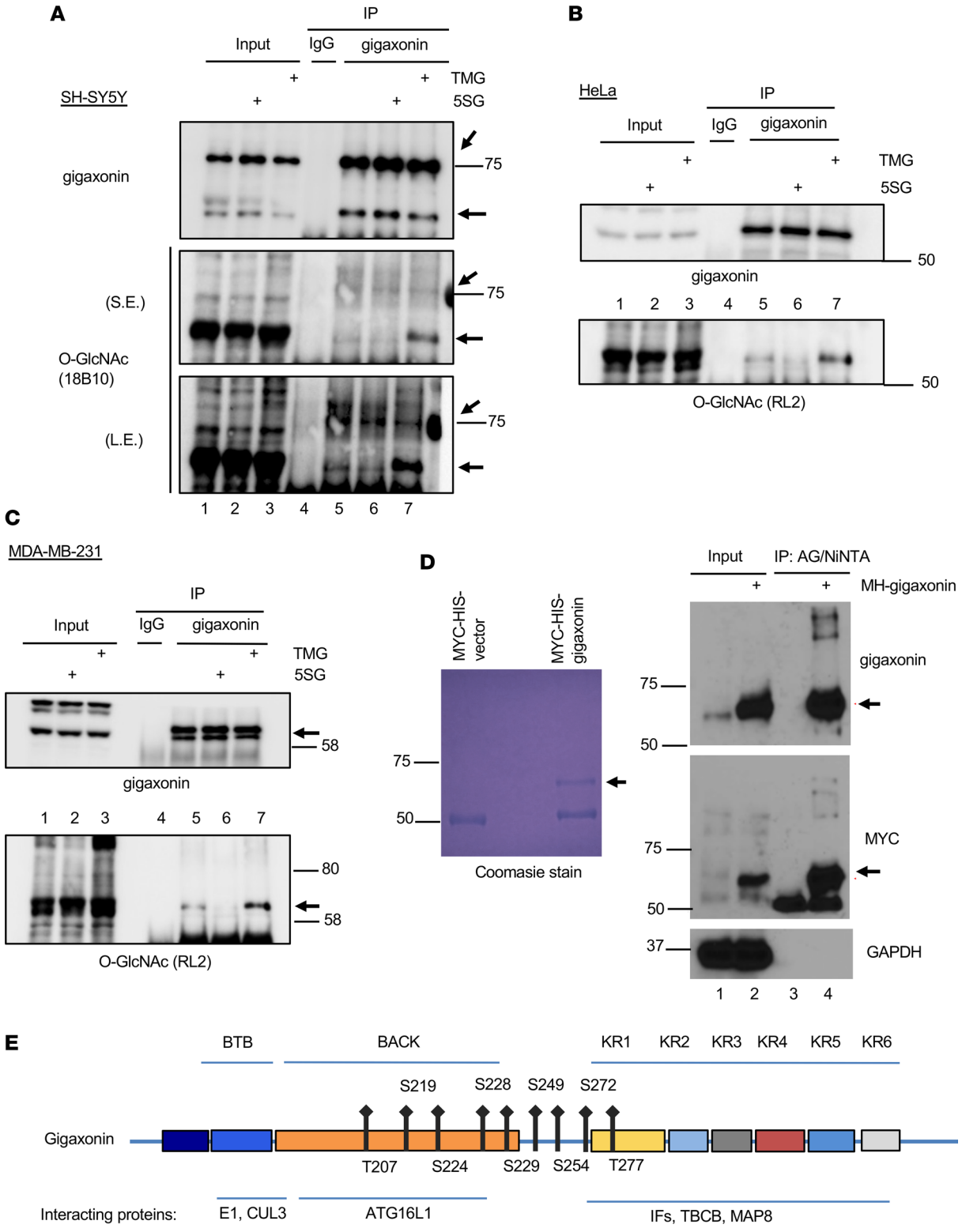

Figure 1. Site-specific O-GlcNAcylation of human gigaxonin. (**A**–**C**) Inhibition of OGT by 50 μM $Ac_4$5SGlcNAc (5SG) or of OGA by 25 μM Thiamet G (TMG) for 24 hours decreases or increases endogenous gigaxonin O-GlcNAcylation, respectively, in SH-SY5Y (S.E: short exposure, 3 minutes; L.E.: long exposure, 6 minutes), HeLa (24 hours), and MDA-MB-231 cells (34 hours) (n = 2). Cells were treated as indicated, and endogenous gigaxonin was immunoprecipitated from whole-cell lysates and analyzed by WB. Gigaxonin bands are indicated by arrows. (**D**) Coomassie blue stain (left) and WB (right) of myc-6xHis–gigaxonin protein tandem purified from 293T cells for MS site mapping (n = 2). (**E**) MS analysis identified 9 candidate O-GlcNAc sites on gigaxonin, indicated in the context of its domain structure and sites of interaction with known binding partners. KR, kelch repeat. Complete gigaxonin site mapping data are available via ProteomeXchange (http://www.proteomexchange.org, dataset identifier PXD012488).

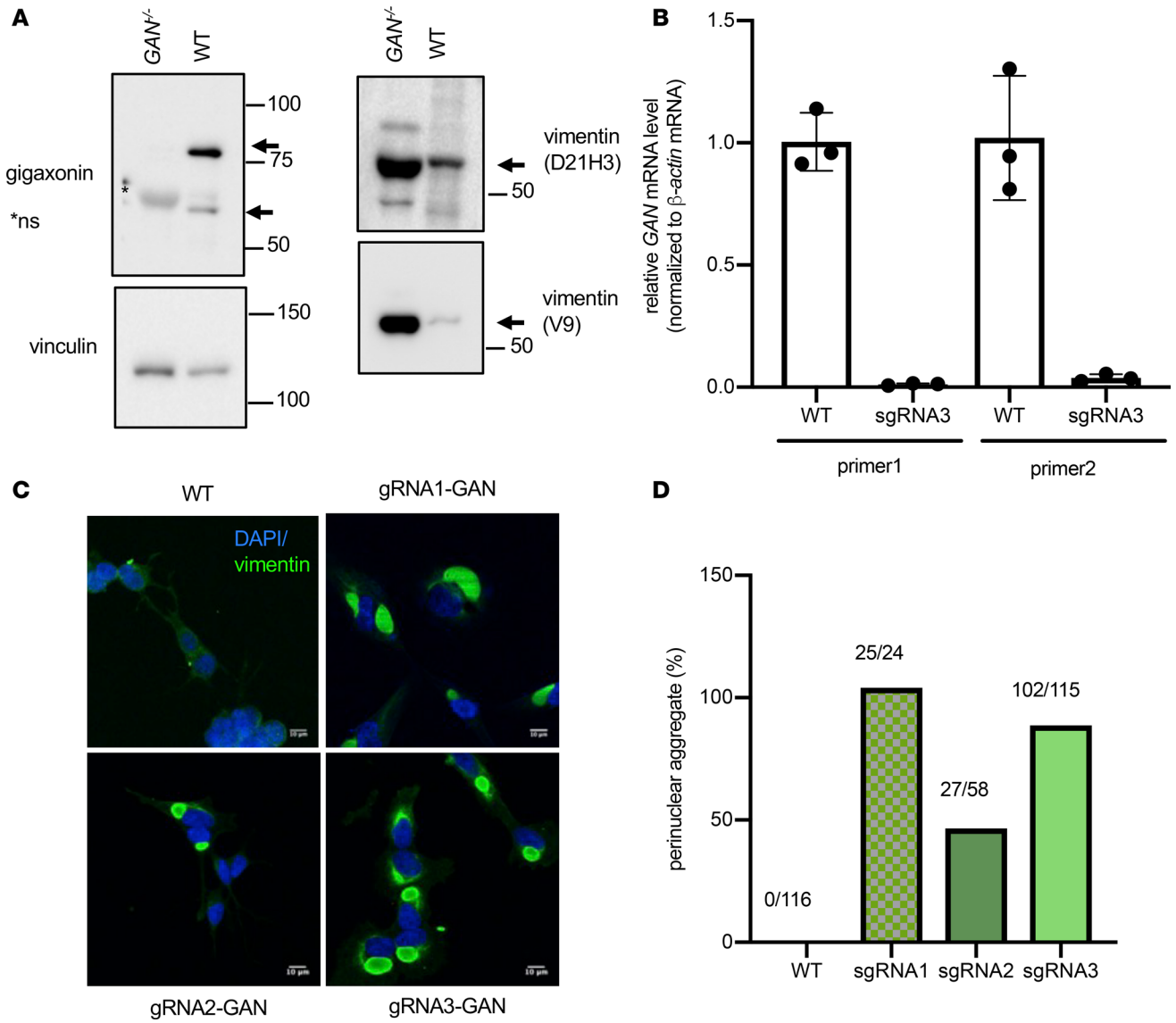

Figure 2. Generation of GAN model cell systems by CRISPR/Cas9 genome engineering. (**A**) SH-SY5Y cells were subjected to control or *GAN* gRNA genome editing. Lysates from single cell–derived clones were analyzed by WB, confirming loss of gigaxonin (arrow) and increased vimentin levels (arrows) in $GAN^{-/-}$ cells, as compared with controls. ns, nonspecific. (**B**) Quantification of *GAN* mRNA expression in control and $GAN^{-/-}$ (gRNA) cells by qPCR (n = 3; black dots represent individual biological replicates). (**C**) Vimentin forms ovoid, perinuclear aggregates in $GAN^{-/-}$ cells. Endogenous vimentin (green) and nuclei (DAPI, blue) were visualized by IFA in control and $GAN^{-/-}$ cells derived from 3 independent gRNAs. Scale bars: 10 μm. (**D**) Quantification of ovoid and perinuclear aggregates in $GAN^{-/-}$ cells. The number of ovoid aggregates and counted cells associated with each sgRNA is shown.

Taken together, these results show that engineered *GAN*-deficient neuroblastoma cell and fibroblast lines phenocopy pathophysiologically relevant characteristics of GAN patient cells (8), indicating that they are tractable and appropriate models for evaluating the function of gigaxonin O-GlcNAcylation.

S272 and T277 O-GlcNAc sites are required for gigaxonin function. To evaluate the functional significance of the gigaxonin O-GlcNAc sites we identified, we harnessed the disease-relevant vimentin aggregation phenotype of $GAN^{-/-}$ cells (Figures 2 and 3) to assess the function of unglycosylatable gigaxonin point mutants. First, we expressed HA-tagged WT or S52G mutant gigaxonin (a known loss-of-function GAN disease allele, as a control; ref. 12) in $GAN^{-/-}$ SH-SY5Y cells and performed IFA. As shown previously, $GAN^{-/-}$ SH-SY5Y cells exhibited dramatically increased vimentin levels compared with controls (Figure 4, upper 2 rows). Reexpression of WT gigaxonin (HA-WT-gigaxonin) markedly repressed vimentin levels (Figure 4, 3rd to 5th rows; Supplemental Figure 3A), whereas the disease-causing S52G mutant did not (Figure 4, 6th row, and Supplemental Figure 3A) (12).

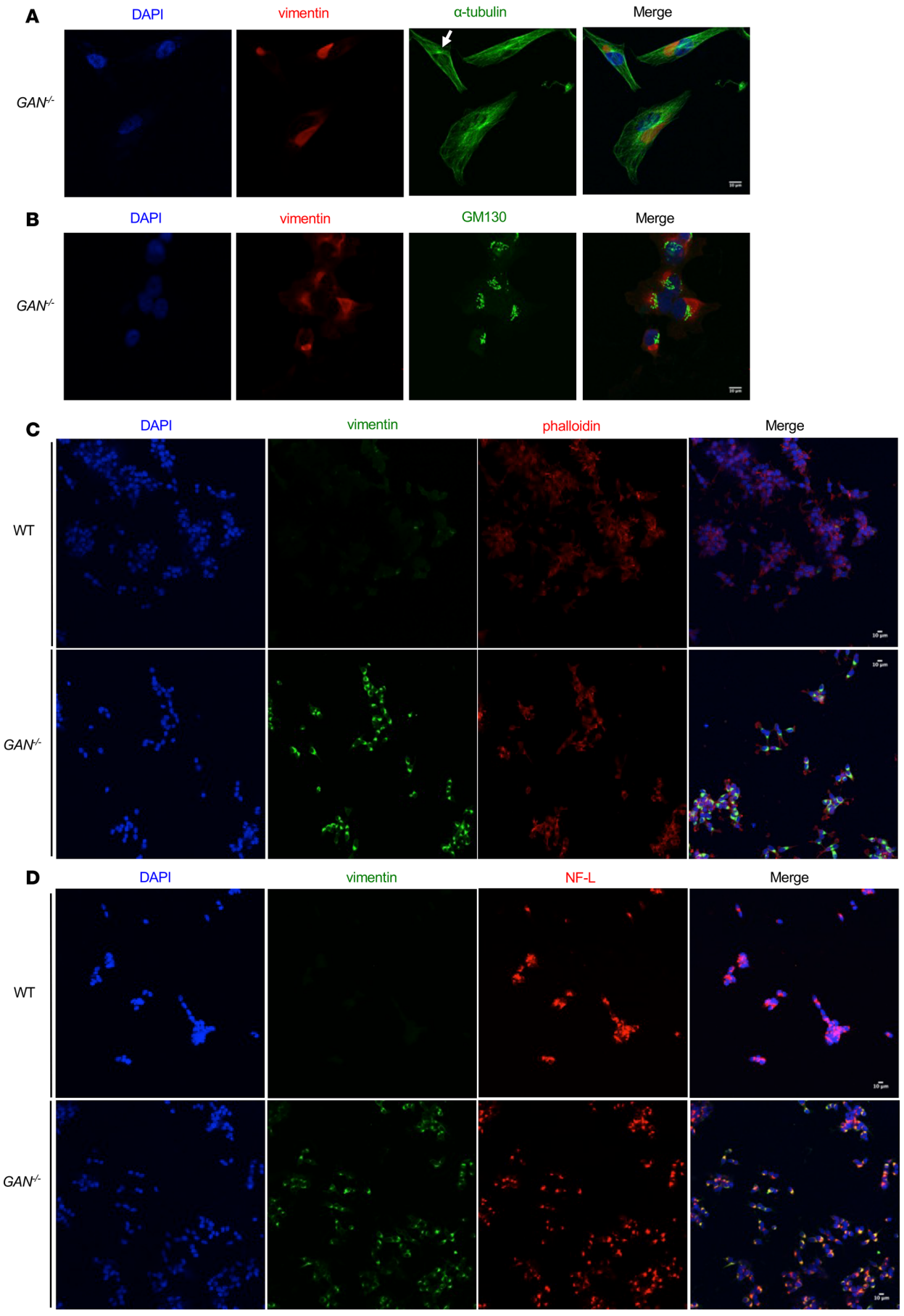
A
DAPI
vimentin
α-tubulin
Merge
GAN-/-
B
DAPI
vimentin
GM130
Merge
GAN-/-
C
DAPI
vimentin
phalloidin
Merge
WT
GAN-/-
D
DAPI
vimentin
NF-L
Merge
WT
GAN-/-

Figure 3. Distribution of vimentin aggregates, F-actin, and NF-L in CRISPR/Cas9-engineered *GAN*$^{-/-}$ cells. (**A**) Vimentin aggregates colocalize with the microtubule organizing center in *GAN*$^{-/-}$ cells, as detected by α-tubulin (white arrow) and vimentin IFA. (**B**) Vimentin aggregates do not colocalize with the Golgi marker GM130, as indicated by IFA in *GAN*$^{-/-}$ cells. Scale bars: 30 μm.(**C**) F-actin distribution is not affected by gigaxonin loss, as indicated by IFA and phalloidin staining in *GAN*$^{-/-}$ cells. (**D**) Colocalization of NF-L and vimentin in *GAN*$^{-/-}$ cells, as indicated by IFA. Scale bars: 10 μm.

These results confirm that the vimentin aggregation phenotype of *GAN*$^{-/-}$ cells is an appropriate assay for assessing the function of WT and mutant gigaxonin.

Next, we used *GAN*$^{-/-}$ cells to test the function of the 9 unglycosylatable gigaxonin point mutants. Interestingly, among all mutants, only S272A and T277A consistently failed to clear or prevent the formation of ovoid bundles, exhibiting a partial loss-of-function phenotype across 3 independent experiments (Figure 5 and Supplemental Figure 3B). We recently reported that vimentin O-GlcNAcylation regulates IF structure and function (55). Therefore, we investigated whether vimentin glycosylation could impact its turnover by WT or mutant gigaxonin as well. We found that WT gigaxonin expression reduced WT vimentin levels more efficiently than S272A or T277A gigaxonin did in EGFP-WT-vimentin–reconstituted vimentin$^{-/-}$ HeLa cells (55) (Figure 6, A and B). In contrast, the unglycosylatable S49A vimentin mutant, which lacks O-GlcNAc at a crucial site (55), is a poorer substrate for WT, S272A, and T277A gigaxonin alike, as compared with WT vimentin (Supplemental Figure 3, C and D). These results indicate that O-GlcNAcylation of gigaxonin substrates may also affect their proteasome-mediated degradation. Therefore, O-GlcNAc signaling may impact the proteostasis of IFs in several ways, an important subject for future studies. With respect to gigaxonin in particular, these data indicate that the S272 and T277 O-GlcNAcylation sites are critical for its ability to regulate IF protein levels. Given that S272 and T277 may also be the primary sites of inducible gigaxonin O-GlcNAcylation (Supplemental Figure 1), the dynamic, site-specific glycosylation of S272 and T277 may be required for normal gigaxonin activity in cells.

Because gigaxonin and CUL3 interact genetically and biochemically, we hypothesized that loss of gigaxonin O-GlcNAcylation at specific sites might affect these functional interactions, by analogy with our prior results with KEAP1 (14). To test this possibility, we coexpressed WT or unglycosylatable gigaxonin mutants with CUL3 in 293T cells and examined their effects on endogenous IF proteins. 293T cells transfect efficiently, express endogenous vimentin and neurofilament (NF), and have served as a tractable and useful model for studying the molecular mechanism of gigaxonin previously, making them an appropriate system for these experiments (12, 49, 56). Overexpression of gigaxonin significantly reduces vimentin levels even in cells that express endogenous gigaxonin (12). CUL3 overexpression alone had no effect on vimentin but coexpression of CUL3 and gigaxonin further reduced vimentin levels, as predicted by their established functional interaction (Supplemental Figure 4A). In contrast, coexpression of the S52G gigaxonin mutant with CUL3 failed to reduce vimentin and NF-L levels, compared with WT gigaxonin (Figure 7A), in agreement with a previous report (12). Consistent with our results in *GAN*$^{-/-}$ cells (Figures 4–6), coexpression of the S272A or T277A mutant with CUL3 failed to reduce vimentin and NF-L levels (Figure 7, A and B). Collectively, these data highlight the importance of the S272 and T277 gigaxonin O-GlcNAcylation sites in governing the degradation of IF proteins.

Gigaxonin O-GlcNAcylation sites are required for interaction with IF proteins. Gigaxonin is thought to be an adaptor for CUL3-containing E3 ligase complexes, mediating the ubiquitination and degradation of IF proteins. Gigaxonin interacts with both CUL3 (7) and the E1 through its BTB domain (57). Truncation mutants and biochemical experiments have demonstrated that the gigaxonin Kelch domains interact with ubiquitination targets, such as tubulin cofactor B (58, 59) and vimentin (49). However, the specific residues on gigaxonin critical for interacting with these targets remain unidentified.

Based on our prior studies of KEAP1 glycosylation (14), we hypothesized that O-GlcNAcylation of gigaxonin might influence its biochemical interactions with CUL3 or with IF proteins themselves. In support of this idea, STRING analysis, based on direct and indirect interactome databases (60), suggested that gigaxonin interacts with several E3 ligase components, including CUL3 and ring box protein 1 (RBX1) (Supplemental Figure 4B) (61). We experimentally reconfirmed the biochemical interaction between endogenous CUL3 and gigaxonin via co-IP and WB (Supplemental Figure 4C). Interestingly, the CUL3-gigaxonin interaction was not affected by the S272A or T277A mutations (Figure 8A, lanes 7 and 8), likely because these residues lie outside the BTB domain thought to interact with CUL3 (7).

Next, we tested whether the interactions between gigaxonin and its substrates vimentin and NF-L were affected by O-GlcNAc site mutations. The molecular weight of endogenous vimentin (54 kDa)

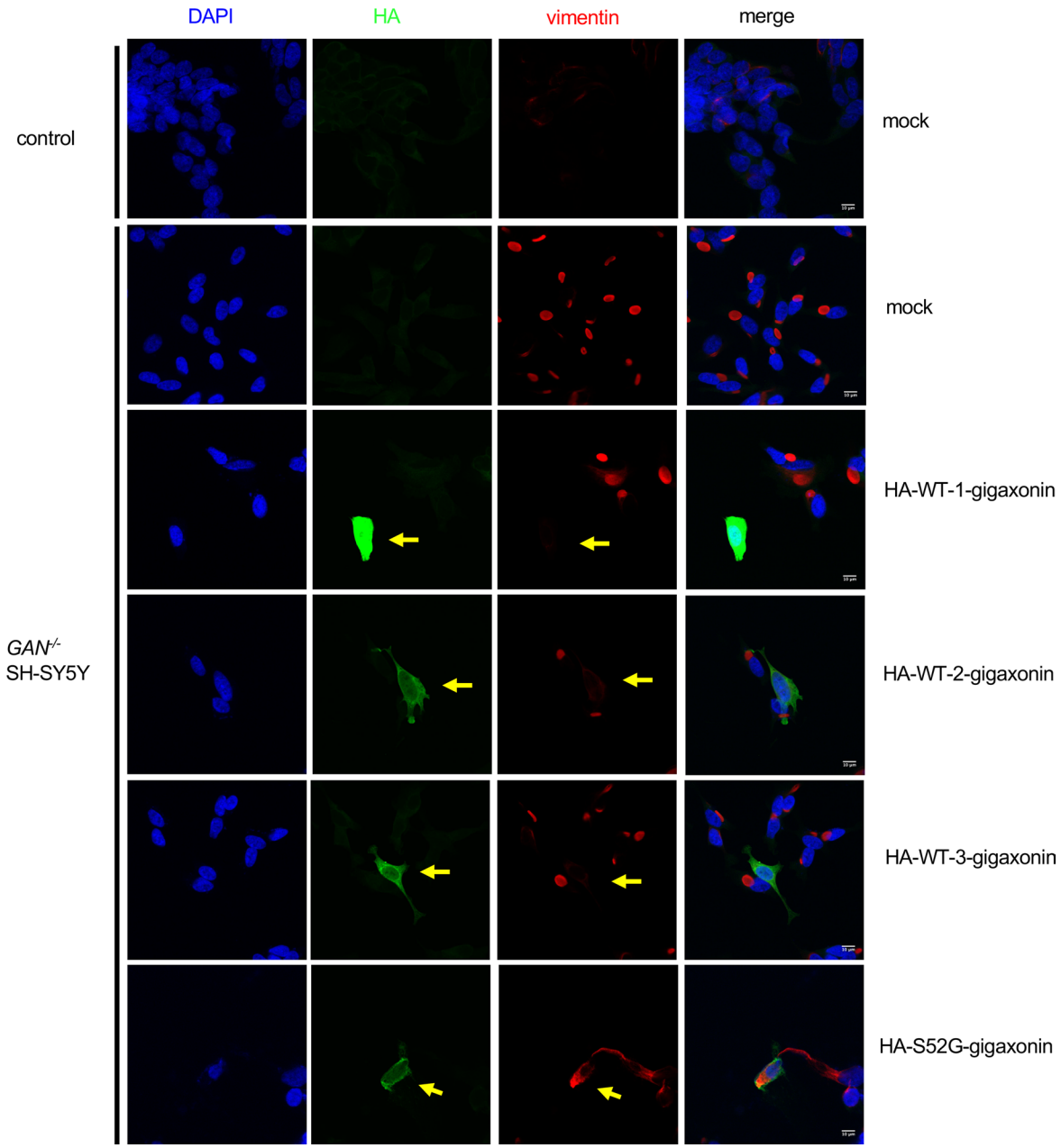

Figure 4. The vimentin aggregation phenotype is an appropriate assay for assessing the function of WT and mutant gigaxonin. Expression of WT gigaxonin, but not the S52G mutant, clears vimentin aggregates in *GAN*$^{-/-}$ cells. Control (top row) or *GAN*$^{-/-}$ (rows 2–6) SH-SY5Y cells were mock transfected or transfected with HA-WT- or HA-S52G-gigaxonin constructs for 72 hours. Expressed gigaxonin (HA, green) and endogenous vimentin (red) were visualized by IFA. Arrows indicate cells expressing HA-gigaxonin (n = 3). Scale bars: 10 μm.

is similar to that of IgG heavy chain, which would complicate the interpretation of IP/WB results. Therefore, we used a previously validated EGFP-vimentin construct (55) for these experiments. EGFP-vimentin and HA-gigaxonin constructs (WT, or S272A or T277A mutant) were cotransfected into 293T cells. Co-IP assays confirmed a robust interaction between WT gigaxonin and EGFP-vimentin, as expected (Figure 8B) (55, 62). However, the interaction between vimentin and S272A or T277A gigaxonin, as compared with WT, was consistently reduced when IP by either HA (gigaxonin) or GFP (vimentin) antibody (Figure 8B, lane 7 vs. 8 or 11 vs. 12). A similarly reduced interaction was also observed between soluble endogenous NF-L and expressed S272A or T277A gigaxonin compared with WT (Figure 8B, lanes 7 and 8, and Figure 8, C and D). Moreover, the S272A and T277A gigaxonin mutants triggered less polyubiquitination of vimentin compared with WT (Figure 8E), indicating a

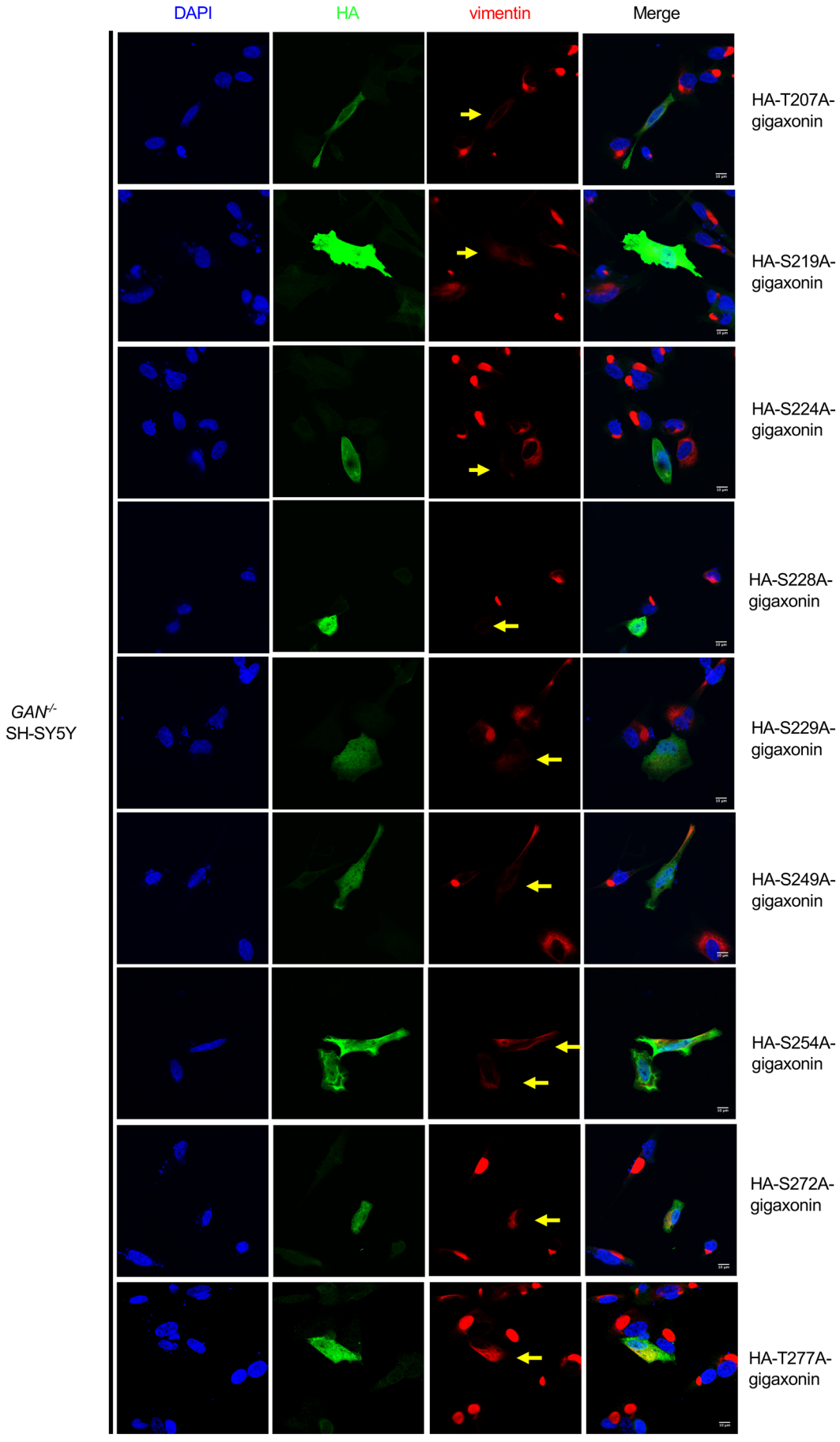

Figure 5. S272A and T277A gigaxonin mutants exhibit the partial loss-of-function phenotype. *GAN*$^{-/-}$ SH-SY5Y cells were transfected with the indicated HA-tagged unglycosylatable gigaxonin point mutant constructs for 72 hours. Expressed gigaxonin (HA, green) and endogenous vimentin (red) were visualized by IFA. Arrows indicate cells expressing HA-gigaxonin (n = 3). Scale bars: 10 μm.

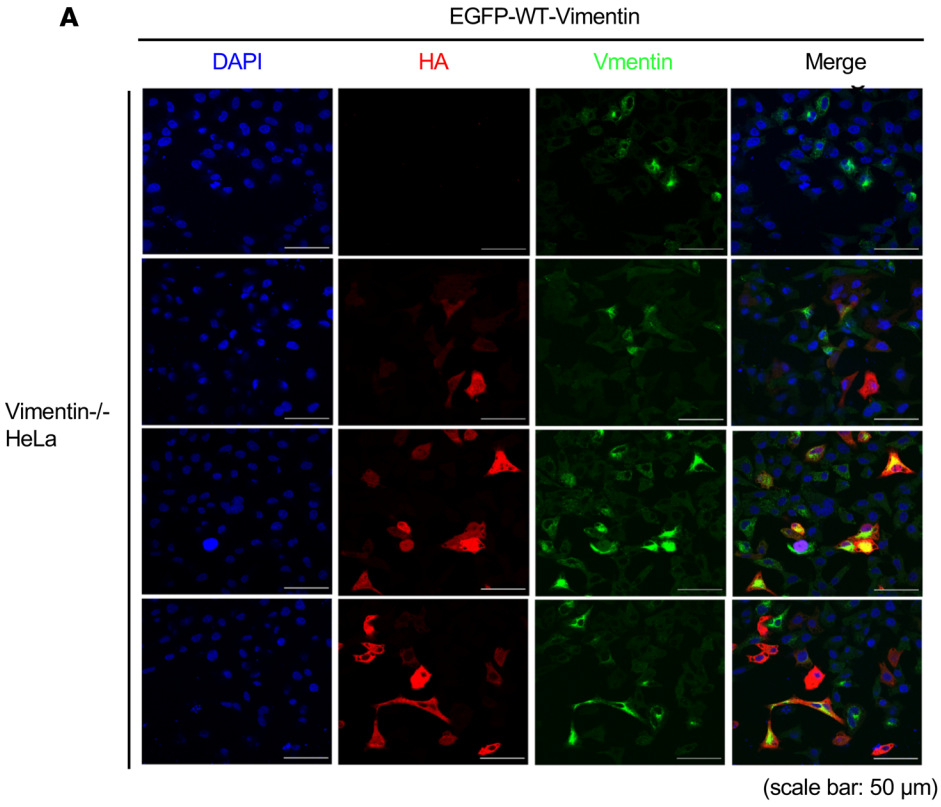

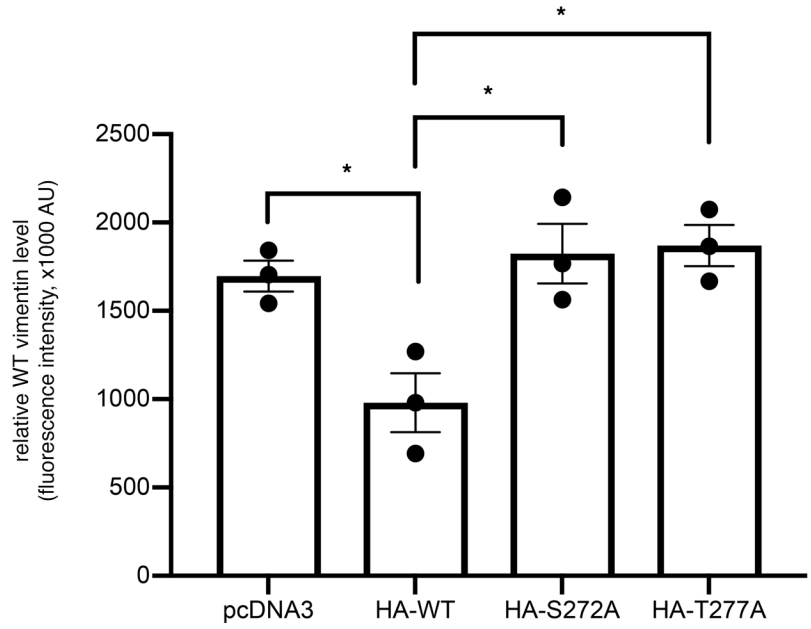

Figure 6. Unglycosylatable S272A and T277A gigaxonin mutants are impaired in clearing vimentin aggregates. (**A**) Vimentin$^{-/-}$ HeLa cells were transfected with the indicated HA-tagged WT or unglycosylatable gigaxonin point mutant constructs for 72 hours. Expressed gigaxonin (HA, red) and endogenous vimentin (green) were visualized by IFA. Compared with WT, S272A- and T277A-gigaxonin exhibited reduced ability to clear EGFP-WT-vimentin. Scale bars: 50 μm. (**B**) Quantification of vimentin in gigaxonin-transfected cells in **A**. Vimentin fluorescence intensity from 80–100 HA-positive cells (or EGFP-positive cells in the pcDNA3 group) was measured, normalized to the HA-positive cell number, and averaged across various fields on each cover glass. The mean values of the experimental groups from 3 biological replicates were analyzed first by 1-way ANOVA and then using Tukey's HSD post hoc test. Data are presented as mean ± SEM; *$P < 0.05$.

functional impact of this reduced biochemical interaction. Together, these data demonstrate that the S272 and T277 gigaxonin glycosylation sites are critical for its optimal interaction with IF proteins, leading to polyubiquitination and protein turnover.

The effects of nutrients and GAN-associated mutations on gigaxonin O-GlcNAcylation. Because O-GlcNAc is a nutrient-sensitive modification (18, 63, 64), we hypothesized that various metabolic conditions might affect gigaxonin O-GlcNAcylation, similar to our prior results with KEAP1 (43, 44). In support of this possibility, Bomont and Koenig showed that the vimentin aggregation observed in *GAN* loss-of-function cells was aggravated by serum starvation or microtubule depolymerization (8), treatments also known to induce global O-GlcNAc changes (59, 65–67). Therefore, we tested whether gigaxonin

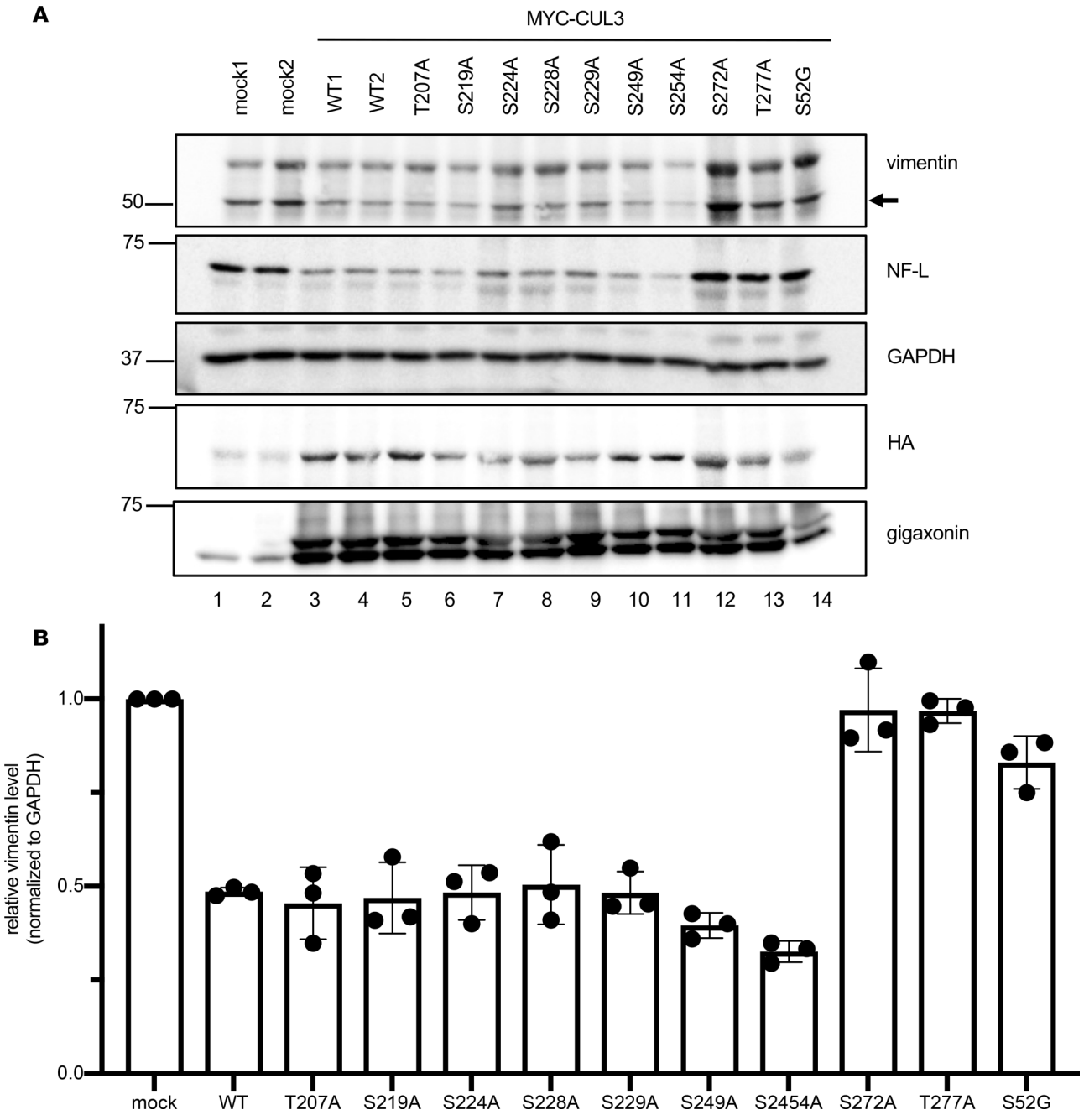

Figure 7. Unglycosylatable S272A and T277A gigaxonin mutants are impaired in cooperating with CUL3 to reduce IF protein levels. (**A**) 293T cells were mock transfected or transfected with MYC-CUL3 and WT or point mutant HA-gigaxonin constructs, as indicated, for 72 hours. Cell lysates were analyzed by WB. (**B**) Quantification of vimentin protein level (normalized to GAPDH level) in mock-, WT-, or indicated point mutant gigaxonin–transfected cells in **A** (*n* = 3; black dots represent individual biological replicates; mean ± SD).

O-GlcNAcylation is impacted by serum starvation. Interestingly, IP/WB experiments revealed that serum starvation consistently reduced gigaxonin glycosylation, as judged by 2 different anti–O-GlcNAc monoclonal antibodies (Figure 9A, lane 4 vs. 5). In the same samples, we also observed accumulation of vimentin under serum starvation (Supplemental Figure 5), reminiscent of the enhanced vimentin aggregation when GAN patient fibroblasts were similarly treated (8). In another independent test of our hypothesis, gigaxonin O-GlcNAcylation was reduced by deprivation of glucose and glutamine (68), essential nutrients feeding the HBP (Figure 9B, lane 5 vs. 6, and Figure 9C). From these results, we concluded that gigaxonin O-GlcNAcylation is responsive to nutrient levels.

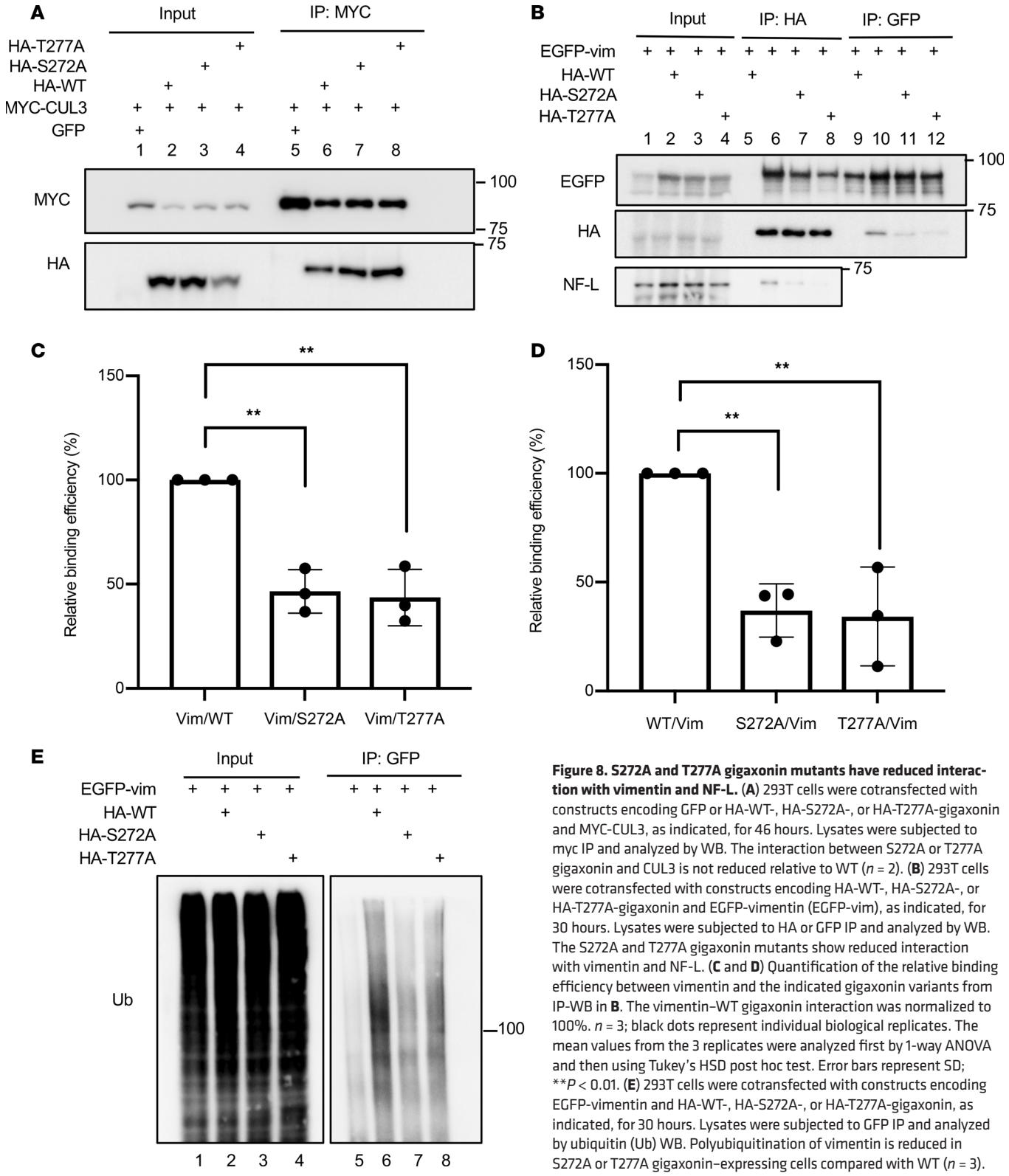

Figure 8. S272A and T277A gigaxonin mutants have reduced interaction with vimentin and NF-L. (**A**) 293T cells were cotransfected with constructs encoding GFP or HA-WT-, HA-S272A-, or HA-T277A-gigaxonin and MYC-CUL3, as indicated, for 46 hours. Lysates were subjected to myc IP and analyzed by WB. The interaction between S272A or T277A gigaxonin and CUL3 is not reduced relative to WT (n = 2). (**B**) 293T cells were cotransfected with constructs encoding HA-WT-, HA-S272A-, or HA-T277A-gigaxonin and EGFP-vimentin (EGFP-vim), as indicated, for 30 hours. Lysates were subjected to HA or GFP IP and analyzed by WB. The S272A and T277A gigaxonin mutants show reduced interaction with vimentin and NF-L. (**C** and **D**) Quantification of the relative binding efficiency between vimentin and the indicated gigaxonin variants from IP-WB in **B**. The vimentin–WT gigaxonin interaction was normalized to 100%. n = 3; black dots represent individual biological replicates. The mean values from the 3 replicates were analyzed first by 1-way ANOVA and then using Tukey's HSD post hoc test. Error bars represent SD; $^{**}P < 0.01$. (**E**) 293T cells were cotransfected with constructs encoding EGFP-vimentin and HA-WT-, HA-S272A-, or HA-T277A-gigaxonin, as indicated, for 30 hours. Lysates were subjected to GFP IP and analyzed by ubiquitin (Ub) WB. Polyubiquitination of vimentin is reduced in S272A or T277A gigaxonin–expressing cells compared with WT (n = 3).

Discussion

Here we report that the KLHL protein gigaxonin is O-GlcNAcylated in a nutrient- and serum-responsive manner. Of 9 candidate O-GlcNAc sites we identified, S272 and T277 were glycosylated and required for gigaxonin's full interaction with, and ubiquitination of, IF proteins. Our loss-of-function *GAN* models display classical ovoid vimentin aggregates in a consistent and robust manner, enabling genetic complementation experiments to

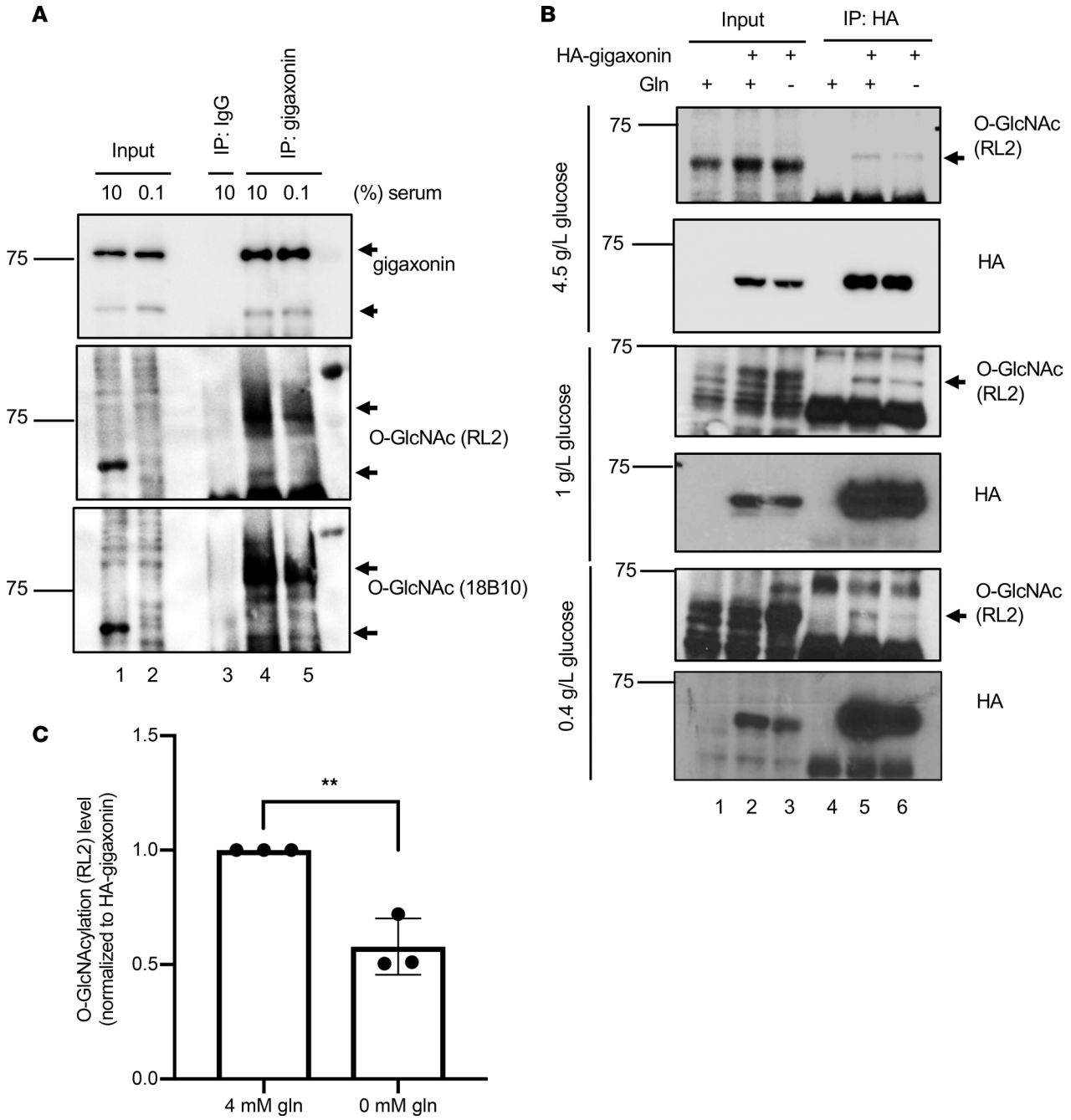

Figure 9. Nutrient-sensitive regulation of gigaxonin O-GlcNAcylation. (**A**) SH-SY5Y cells were treated with 10% or 0.1% serum for 72 hours, as indicated, and lysed. Endogenous gigaxonin was immunoprecipitated and analyzed by WB. Gigaxonin O-GlcNAcylation is reduced after serum starvation, as indicated by 2 different anti–O-GlcNAc monoclonal antibodies (representative results from 3 biological replicates). Arrows indicate gigaxonin bands. (**B**) 293T cells were transfected with WT HA-gigaxonin for 24 hours, treated with control (4 mM) or glutamine-free medium for an additional 48 hours under various glucose concentrations, as indicated, and then lysed. HA-gigaxonin was immunoprecipitated and analyzed by WB. Gigaxonin O-GlcNAcylation is reduced after glutamine starvation under low-glucose conditions, as indicated by anti–O-GlcNAc (RL2) WB. Arrows indicate gigaxonin bands. (**C**) Quantification of gigaxonin glycosylation under glutamine (gln) starvation and low-glucose conditions (0.4 g/L) in **B** (n = 3; black dots represent individual biological replicates; mean ± SD; Student's t test, $^{**}P < 0.01$).

measure the impact of individual point mutations on IF protein turnover. These experiments further confirmed the functional significance of the S272 and T277 O-GlcNAc sites. Together, our results suggest that stimulus-induced O-GlcNAcylation of gigaxonin may be required for its optimal ability to regulate IF protein turnover, perhaps by inducing a conformational change in gigaxonin that promotes IF protein binding (Figure 10).

Culture models of GAN. Current models for GAN rely primarily on patient-derived fibroblasts (8, 12, 50), induced pluripotent stem cells (69), or *GAN*$^{-/-}$ mice (13, 51–53). Though valuable, patient-derived

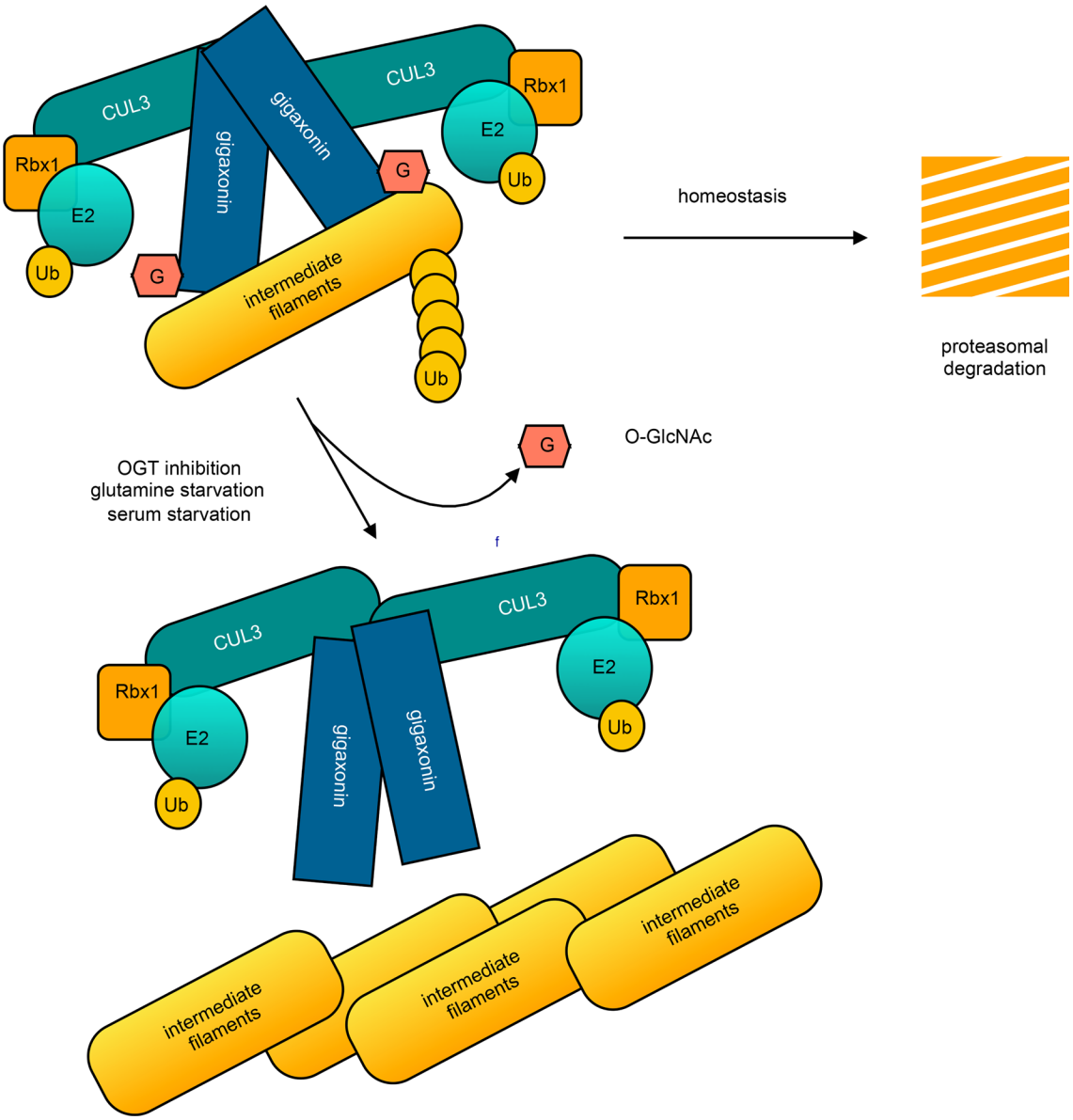

Figure 10. Proposed model for O-GlcNAc–mediated regulation of gigaxonin. Taken together, our results suggest that O-GlcNAcylation of gigaxonin promotes its optimal interaction with IF proteins (e.g., vimentin or NF-L) to facilitate their polyubiquitination and proteasome-mediated degradation. Nutrient deprivation and/or other stimuli lead to reduced gigaxonin O-GlcNAcylation, especially at S272 and T277, inhibiting its interaction with IFs and leading to their accumulation.

cells have heterogeneous genetic backgrounds and display incompletely penetrant IF phenotypes (e.g., 3%–15% of cells displaying ovoid aggregates), which may complicate the interpretation of mechanistic and functional studies. *GAN*$^{-/-}$ mice have also been powerful systems but do not fully phenocopy human GAN symptoms, suggesting important species-dependent differences (13, 51–53). Using CRISPR-mediated gene deletion, we developed *GAN*$^{-/-}$ models in both GAN-relevant human fibroblast and neuroblastoma cell lines (12), in which more than 80% of *GAN*$^{-/-}$ cells display ovoid-shaped vimentin aggregates (Figure 2 and Figure 3). These human *GAN*$^{-/-}$ cell lines are easier to propagate and manipulate experimentally than are patient-derived cells or mice, and are therefore expected to complement existing systems and facilitate the characterization of the biochemical regulation of gigaxonin and IF aggregation. Importantly, our cell systems may also enable future high-throughput chemical or genetic screens to identify candidate drugs and drug targets to ameliorate IF protein aggregation in GAN.

Gigaxonin O-GlcNAc sites in human disease. While our findings await investigation in other physiologically and clinically relevant systems (e.g., rodent models, primary neuronal cultures, GAN patient cells), our current

results suggest novel hypotheses to test in GAN disease contexts. For example, gigaxonin O-GlcNAcylation might be dysregulated in GAN patients, leading to reduced gigaxonin stability or reduced interaction with, and ubiquitination of, IF proteins and/or other recently discovered gigaxonin substrates involved in autophagy (48) and sonic hedgehog signaling (70). While none of the 9 identified candidate O-GlcNAc sites is reported to be mutated in the GAN patients sequenced to date, it is still possible that GAN disease allele mutations at other sites may affect O-GlcNAcylation by inducing conformational changes that affect the access of OGT or OGA. More work will be required to gain mechanistic insight into how O-GlcNAcylation regulates gigaxonin function in GAN-relevant contexts. For instance, it will be important to analyze the O-GlcNAcylation status of gigaxonin in human patients, which may be helpful in predicting protein function in vivo.

GAN$^{-/-}$ SH-SY5Y cells exhibit reduced proliferation and often grow as individual cells, rather than clusters, suggesting that gigaxonin may play a role in cancer-relevant phenotypes. To date, 276 different gigaxonin somatic mutations have been identified in human tumor samples in the cBioPortal database (https://www.cbioportal.org/) (71, 72). Among these, 2 alter O-GlcNAc sites: an S272F mutation was identified in a cutaneous melanoma and an S254C mutation in prostate adenocarcinoma. Our results predict that the S272F mutation, at least, would impair gigaxonin function. IFs — especially vimentin — participate in multiple cancer-relevant processes, including cell adhesion, migration, epithelial-mesenchymal transition, and metastasis (73, 74). Therefore, the biological significance of gigaxonin in cancer or other diseases may be underappreciated, and the function of gigaxonin in tumor biology could be an interesting subject of future work (75).

Nutrient sensing and O-GlcNAcylation as potential modifiers of gigaxonin function and GAN phenotypes. Nutrient sensing is thought to be a prominent function of O-GlcNAcylation in intracellular signaling (16, 19–24, 26, 27, 29). In a previous study, we reported that O-GlcNAcylation of the KLHL protein KEAP1 varies dynamically with glucose levels (14). Given these results, it is intriguing that gigaxonin O-GlcNAcylation also fluctuates with metabolic cues (Figure 9). Together, these observations suggest that nutrient status and IF proteostasis might be linked through the glycosylation of gigaxonin in particular, and that O-GlcNAcylation may be a widespread regulatory modification of KLHL proteins in general.

Here we show that deprivation of serum or glucose and glutamine (which feed the HBP) reduces gigaxonin O-GlcNAcylation (Figure 9). Interestingly, serum starvation was previously reported to potentiate IF aggregation in *GAN* loss-of-function cells, but the underlying mechanism remained unclear (8). Recently, ATG16L-1, a key factor for phagophore formation, was identified as a novel gigaxonin substrate (48), suggesting another potential connection among nutrient starvation, autophagy, and gigaxonin function. In the future, it will be interesting to determine whether gigaxonin O-GlcNAcylation impacts ATG16L-1 and autophagy. We propose that nutrient or growth factor starvation may trigger gigaxonin deglycosylation, reducing its interaction with its substrates, such as vimentin or NF-L, and eventually leading to IF accumulation and aggregation (Figure 10). However, serum starvation induces a variety of signaling events that may directly or indirectly regulate OGT, OGA, or UDP-GlcNAc availability, including the glycosylation of IF proteins themselves. The influence of these factors on the O-GlcNAcylation, regulation, and function of gigaxonin will be a key focus of future studies. In the longer term, it will be important to determine whether changes in metabolic cues and gigaxonin glycosylation affect its function in vivo, and whether this signaling is dysregulated in GAN patients, potentially contributing to the variability of disease severity.

Therapeutic implications. Finally, although they must be further validated in clinically relevant models, our findings may have important implications for GAN therapy. Currently, there are no treatments to mitigate symptoms or disease progression, due partly to our imperfect understanding of the molecular etiology of GAN. However, gene therapy approaches have shown significant potential. For example, Gray and colleagues used engineered adeno-associated virus (AAV) vectors to restore WT gigaxonin expression in *GAN*$^{-/-}$ mice and achieved persistent transgene expression in the central and peripheral nervous systems for more than 1 year, accompanied by reduced neuronal IF protein aggregation (76). More recently, the Gray laboratory conducted clinical trials of intrathecal delivery of a scAAV9/JeT-GAN vector to reexpress WT gigaxonin in GAN patients (NCT02362438). Despite this clear promise, potential obstacles remain. For example, endogenous gigaxonin is normally expressed at low levels, and its ectopic overexpression obliterates the entire IF network, leading to cell dysfunction (11, 12). Therefore, improved knowledge of gigaxonin regulation — through O-GlcNAcylation and other mechanisms — is needed to understand its activity in healthy neurons and, perhaps, to tune its activity during GAN gene therapy (47, 77).

Methods

Cell culture. SH-SY5Y, 293T, HeLa, and MDA-MB-231 cell lines were obtained from the Duke Cell Culture Facility (CCF) and the BJ5ta cell line was obtained from ATCC. Media used were as follows: for SH-SY5Y cells, DMEM/F-12 (Gibco 11320) with HEPES (Gibco 15630); HeLa, 293T, and MDA-MB-231, DMEM (Gibco 11995) with HEPES; and BJ5ta, 4:1 ratio of DMEM (Gibco 11965) and Medium 199 (Gibco 11150). All cell lines were maintained at 37°C in a 5% CO_2 atmosphere following standard guidelines of the Duke CCF or ATCC, and were cultured in medium supplemented with 10% FBS and penicillin/streptomycin. For serum starvation, SH-SY5Y cells were first washed twice with PBS and then treated with medium containing 10% or 0.1% FBS for 72 hours (8). For glutamine deprivation, HA-gigaxonin–transfected (24 hours, total DNA: 10 μg per 10-cm plate) 293T cells were first washed twice with PBS and then transferred to medium (Gibco A1443001; 10% dialyzed FBS, MilliporeSigma F0392; glucose, Thermo Fisher Scientific A2494001; sodium pyruvate, Thermo Fisher Scientific 11360070) with or without L-glutamine (Gibco 25030081) for an additional 48 hours before collection of lysates.

Preparation of gigaxonin–myc-6xHis protein. Gigaxonin–myc-6xHis expression plasmid or control vector was transfected into 293T cells (15-cm plates × 6 for each condition). For transfection, each 15-cm plate was transfected with 45 μL Mirus TransIT-293 Transfection Reagent, 15 μg DNA (gigaxonin or vector), and 750 μL Opti-MEM (Gibco, catalog 11058021). After 41 hours of transfection, 293T cells were treated with 50 μM Thiamet G and 4 mM glucosamine for an additional 7 hours. To collect lysates, cells were washed with cold PBS twice, and harvested in 4 mL IP lysis buffer (0.1% SDS, 1% Triton X-100, 150 mM NaCl, 1 mM EDTA, 20 mM Tris pH 7.4) in the presence of protease inhibitors and 5 μM PUGNAc (Cayman Chemical, catalog 17151). After measuring protein concentration by BCA assay, an IP (25 mg protein at 2 mg/mL and 25 μg myc antibody clone 9E10, BioLegend 626801) was rotated at 4°C overnight. The next day, 100 μL A/G beads slurry (prewashed with IP lysis buffer) was added into each sample and rotated at room temperature (RT) for 2 hours. After Myc-IP, the beads were then washed with 1 mL IP lysis buffer 4 times, and the proteins were rotated and eluted with 300 μL buffer A (8 M urea, 300 mM NaCl, 1%Triton X-100, and 5 mM imidazole) at RT for 15 minutes. Next, the eluted proteins were incubated with Ni-NTA beads (100 μL slurry preequilibrated) and washed (3 times) with buffer A for 2 hours at RT. The Ni-NTA beads were then washed 4 times with buffer A, and proteins were eluted with 80 μL elution buffer (8 M urea and 250 mM imidazole).

Liquid chromatography–tandem MS analysis of gigaxonin O-GlcNAcylation. Purified gigaxonin–myc-6xHis was separated by SDS-PAGE and Coomassie stained. Stained bands of the correct molecular weight were subjected to standard in-gel trypsin digestion according to a Duke Center for Genomic and Computational Biology protocol (https://genome.duke.edu/sites/genome.duke.edu/files/In-gelDigestionProtocolrevised_0.pdf). Extracted peptides were lyophilized to dryness and resuspended in 12 μL of 0.2% formic acid/2% acetonitrile. Each sample was subjected to chromatographic separation on a Waters NanoAquity UPLC equipped with a 1.7 μm BEH130 C_{18} 75 μm I.D. × 250 mm reversed-phase column. The mobile phase consisted of (A) 0.1% formic acid in water and (B) 0.1% formic acid in acetonitrile. Following a 4-μL injection, peptides were trapped for 3 minutes on a 5 μm Symmetry C_{18} 180 μm I.D. × 20 mm column at 5 μL/min in 99.9% A. The analytical column was then switched in-line, and a linear elution gradient of 5% B to 40% B was performed over 60 minutes at 400 nL/min. The analytical column was connected to a fused silica PicoTip emitter (New Objective) with a 10-μm tip orifice and coupled to a QExactive Plus mass spectrometer (Thermo Scientific) through an electrospray interface operating in data-dependent acquisition mode. The instrument was set to acquire a precursor MS scan from *m/z* 350 to 1800 every 3 seconds. In data-dependent mode, MS/MS scans of the most abundant precursors were collected following higher-energy collisional dissociation (HCD) fragmentation at an HCD collision energy of 27%. Within the MS/MS spectra, if any diagnostic O-GlcNAc fragment ions (*m/z* 204.0867, 138.0545, or 366.1396) were observed, a second MS/MS spectrum of the precursor was acquired with electron transfer dissociation (ETD)/HCD fragmentation using charge-dependent ETD reaction times and either 30% or 15% supplemental collision energy for precursor charge states of at least +2. For all experiments, a 60-second dynamic exclusion was employed for previously fragmented precursor ions.

Raw liquid chromatography–tandem MS (LC-MS/MS) data files were processed in Proteome Discoverer (Thermo Fisher Scientific) and then submitted to independent Mascot searches (Matrix Science) against a SwissProt database (human taxonomy) containing both forward and reverse entries of each protein (https://www.uniprot.org/proteomes/UP000005640) (20,322 forward entries). Search tolerances were 5 ppm for precursor ions and 0.02 Da for product ions using semi-trypsin specificity with up to 2 missed cleavages. Both y/b-type HCD and c/z-type ETD fragment ions were allowed for

interpreting all spectra. Carbamidomethylation (+57.0214 Da on C) was set as a fixed modification, whereas oxidation (+15.9949 Da on M) and O-GlcNAc (+203.0794 Da on S/T) were considered dynamic mass modifications. All searched spectra were imported into Scaffold (v4.3, Proteome Software), and scoring thresholds were set to achieve a peptide FDR of 1% using the PeptideProphet algorithm (http://peptideprophet.sourceforge.net/). When satisfactory ETD fragmentation was not obtained, HCD fragmentation was used to determine O-GlcNAc residue modification using the number of HexNAcs identified in combination with the number of serines and threonines in the peptide.

The MS proteomics data have been deposited to the ProteomeXchange Consortium (78) via the PRIDE (79) partner repository with the dataset identifier PXD012488.

CRISPR, qPCR, and shRNA. To generate *GAN*-knockout models, the lentiviral CRISPR/Cas9 system developed by the Zhang laboratory was used (Addgene 52961) (80). Three different gRNAs targeting the human *GAN* gene were selected using the CHOPCHOP website (http://chopchop.cbu.uib.no) (gRNA1: GCAGAAGAACATCCTGGCGG, gRNA2: GGTGCAGAAGAACATCCTGG, gRNA3: CGGCCAGCCCGTACATCAGG). SH-SY5Y and BJ5ta cells were infected with gRNA/Cas9-expressing lentivirus and selected with puromycin to generate *GAN*-deficient cell lines. The expression of gigaxonin and Cas9 was validated by WB after puromycin selection. $GAN^{-/-}$ cell lines were maintained in puromycin-containing media. To evaluate *GAN* mRNA levels, $GAN^{-/-}$ or parental SH-SY5Y cells were lysed to collect RNAs by RNeasy kit (QIAGEN). *GAN* cDNAs from each group were made using reverse transcriptase II (Thermo Fisher Scientific) and quantified by qPCR. The qPCR primer pairs were designed to target different regions of *GAN* mRNA (168-F: 5′-CCCGGTGCAGAAGAACATCC; 168-R: 5′-AGCCTGATCTGCCCACTGAA; 180-F: 5′-CCAGCCCGTACATCAGGACA180-R: 5′-GGTCAGCTGCCTGAACAACA). The relative level of *GAN* mRNA was normalized to β-actin mRNA in each group.

To knock down *GAN* expression, we used a lentiviral shRNA system from MilliporeSigma (TRCN0000083858), targeting the *GAN* 3′ UTR, with shRNA CCGGCCACATAATATGGGATGCAATCTCGAGATTGCATCCCATATTATGTGGTTTTTG.

IFA. To visualize IFs, control or $GAN^{-/-}$ cells were seeded onto chamber slides (Thermo Fisher Scientific) and transfected using Lipofectamine 3000 (Invitrogen) for 72 hours. Cells were fixed in 4% formaldehyde for 10 minutes, followed by 3 washes with 1× PBS, blocking at RT for 1 hour (5% BSA in 1× PBS, 0.3% Triton X-100), and incubation with anti-vimentin (Cell Signaling Technology 5741, 1:200 in blocking solution) or anti-HA (Santa Cruz Biotechnology Inc. sc-7392, 1:100 in blocking solution) antibody at 4°C overnight. Nuclei were marked by DAPI (Thermo Fisher Scientific S36938), and F-actin was visualized by phalloidin staining (Alexa Fluor 594 Phalloidin, Thermo Fisher Scientific A12381), if applied. The above staining protocol was also applied for NEFL (Cell Signaling Technology 2837, 1:100), GM130 (Cell Signaling Technology 12480, 1:100), and the V5 epitope tag (Cell Signaling Technology 13202, 1:100). All images were acquired on a Zeiss 780 inverted confocal microscope at the Duke Light Microscopy Core Facility.

To visualize gigaxonin and vimentin in the HeLa $Vimentin^{-/-}$ background, 200,000 HeLa $vimentin^{-/-}$ cells (55) were seeded in 6-well plates with a 22-mm coverslip at the bottom of each well. TransIT-LT1 Transfection Reagent (18 μL; Mirus) was added to 250 μL Opti-MEM I (Life Technologies), vortexed briefly, and incubated at RT for 15 minutes. Then, 3 μg of one DNA from list 1 and list 2 (i.e., 6 μg of DNA total) was added to the mixture — list 1: pLenti6 Neo (negative control), EGFP-WT-vimentin, or EGFP-S49A-vimentin; list 2: pcDNA3 (negative control), HA-WT-gigaxonin, HA-S272A-gigaxonin, or HA-T277A-gigaxonin. DNA mixtures were vortexed briefly and incubated at RT for 15 minutes before transfection.

Seventy-two hours after transfection, cells were washed twice with 37°C PBS, fixed with 4% paraformaldehyde (MilliporeSigma) gently on a shaker at RT for 20 minutes, permeabilized with 0.1% Triton X-100 (in PBS) with gentle shaking for 10 minutes, and incubated in blocking buffer (1% BSA in PBS) with rotation at RT for at least 30 minutes. Coverslips were coincubated with vimentin (Cell Signaling Technology D21H3, 1:100) and HA (F-7, Santa Cruz Biotechnology Inc. sc-7392, 1:100) antibodies at 4°C overnight. Cells were washed 3 times with PBS and coincubated with a goat anti-mouse (H + L) Alexa Fluor 594– (Thermo Fisher Scientific A-11005, 1:200) and a goat anti-rabbit (H + L) Alexa Fluor 488–conjugated secondary antibody (Thermo Fisher Scientific A-11008, 1:200) at RT for 1 hour in the dark. Coverslips were washed with PBS 3 times and mounted in ProLong Diamond antifade mounting medium with DAPI (Invitrogen P36931) on cover slides. Images were acquired using a sequential scan (multitrack) using a bandpass emission filter at 410–484 nm for DAPI, 489–561 nm for vimentin, and 585–733 nm for HA on a Zeiss LSM 780 confocal laser scanning microscope fitted with an oil Plan-Apochromat 40×/1.4 numerical aperture objective lens.

Gigaxonin-transfected cells were defined by setting a predetermined HA signal brightness threshold using the Fiji ImageJ particle analysis plugin. Vimentin fluorescence intensity from a total of 80–100 cells with HA-positive signal was measured, normalized to the HA-positive cell number, and averaged across various fields on each cover glass. The mean values between the experimental groups from 3 biological replicates were compared using Student's *t* tests. Error bars representing SEM were included in the bar graphs. A *P* value less than 0.05 was considered statistically significant.

WB and IP. To measure vimentin levels after genetic or chemical manipulation, cells were lysed in RIPA buffer (Thermo Fisher Scientific; 25 mM Tris-HCl pH 7.6, 150 mM NaCl, 1% NP-40, 1% sodium deoxycholate, 0.1% SDS). Whole-cell lysates were sonicated (>20 pulses) on ice until all insoluble material was dissolved. Protein concentrations were determined by BCA assay and used to normalize all samples. After boiling in sample buffer, the lysates were analyzed by WB. For most co-IP experiments, cells were lysed in Pierce IP buffer (1% Triton X-100, 150 mM NaCl, 1 mM EDTA, and 25 mM Tris-HCl pH 7.5) supplemented with protease and phosphatase inhibitors. 250–500 μg (final volume: 250 μL; 1–2 μg/μL) protein lysates were used for IPs. For co-IP of EGFP-vimentin and HA-gigaxonin, cells were transfected with the indicated constructs (total DNA: 10 μg per 10-cm plate) for 24 hours and lysed in Pierce IP buffer. Lysates were sonicated gently (15 pulses) to disrupt aggregates and spun down at 4°C to collect the soluble fraction. Soluble protein extract (500 μg) was incubated with HA or GFP antibody for 6 hours before addition of Dynabeads (Thermo Fisher Scientific) for an overnight incubation at 4°C. Beads were washed 4–5 times with Pierce IP buffer. After washing, samples were eluted in 2× sample buffer at 95°C for 5 minutes. Antibodies used included CUL3 (Bethyl A301-109A), O-GlcNAc (RL2, Santa Cruz Biotechnology Inc. sc-59624s; 18B10.C7, Thermo Fisher Scientific MA1-038), β-tubulin (Cell Signaling Technology 2128), Flag (MilliporeSigma F1840), myc (Santa Cruz Biotechnology Inc. sc-40), HA (Santa Cruz Biotechnology Inc. sc-7392), ubiquitin (Santa Cruz Biotechnology Inc. sc-8017), gigaxonin (MilliporeSigma SAB4200104), NEFL (Cell Signaling Technology 2837), vimentin (Cell Signaling Technology 5741), vinculin (Santa Cruz Biotechnology Inc. sc-73614), GAPDH (Santa Cruz Biotechnology Inc. sc-25778), and GFP (Santa Cruz Biotechnology Inc. sc-8334).

Statistics. For Figure 6B, Supplemental Figure 3D, and Figure 8, C and D, quantitative data were initially analyzed by 1-way ANOVA to minimize the probability of type I errors that might otherwise occur from multiple tests performed on the same data set. The independent variables for the ANOVA were either genotype (pcDNA3, WT-, S272A-, or T277A-gigaxonin) or a ratio of genotypes (vimentin/WT-, S272A-, or T277A-gigaxonin, or WT-, S272A-, or T277A-gigaxonin/vimentin); and the dependent variables were either fluorescence intensity or relative binding efficiency. Following ANOVA, a Tukey's HSD post hoc test was performed on the data because sample sizes were equal between groups and in order to utilize a multiple comparison adjustment in calculating *P* values. Both the ANOVAs and Tukey's HSD post hoc tests were calculated using JMP (version 14.0. SAS Institute Inc., 1989–2019). For Figure 9C, Student's *t* test (2 tailed) was used to obtain the *P* value. $P < 0.05$ was considered significant.

Study approval. Study approval was not required because no animal or human specimens were used in this study.

Author contributions

PHC, JH, JW, DTH, TJS, SP, BJB, ABS, and AL performed the experiments. BMC performed the statistical analysis and provided technical support for imaging analysis. PHC, JTC, and MB designed the experiments and interpreted the results. PHC, JTC, and MB wrote the manuscript. All authors reviewed and approved the manuscript. JTC and MB supervised all aspects of the work.

Acknowledgments

We thank the members of the MB and JTC laboratories for critical discussion and technical support. We also thank Erik Soderblom and the Duke Proteomics and Metabolomics Shared Resource for O-GlcNAc site-mapping analyses. This study was supported by NIH grants 1R01NS111588-01A1 (to JTC and MB), 5R01GM118847 (to MB), R01GM124062 (to JTC); Department of Defense grants W81XWH-17-1-0143, W81XWH-15-1-0486, and W81XWH-19-1-0842 (to JTC); the Duke Cancer Institute pilot fund (to MB and JTC); and a gift from the Hannah's Hope Fund (to MB and JTC).

Address correspondence to: Jen-Tsan Chi, 101 Science Drive, 2177A CIEMAS, Box 3382, Durham, North Carolina 27708, USA; Phone: 919.668.4759; Email: jentsan.chi@duke.edu. Or to: Michael Boyce, Box 3711 DUMC, Durham, North Carolina 27710, USA. Phone: 919.684.9906; Email: michael.boyce@duke.edu.

1. Gordon N. Giant axonal neuropathy. *Dev Med Child Neurol*. 2004;46(10):717–719.
2. Bomont P, et al. The gene encoding gigaxonin, a new member of the cytoskeletal BTB/kelch repeat family, is mutated in giant axonal neuropathy. *Nat Genet*. 2000;26(3):370–374.
3. Berg BO, Rosenberg SH, Asbury AK. Giant axonal neuropathy. *Pediatrics*. 1972;49(6):894–899.
4. Asbury AK, Gale MK, Cox SC, Baringer JR, Berg BO. Giant axonal neuropathy — a unique case with segmental neurofilamentous masses. *Acta Neuropathol*. 1972;20(3):237–247.
5. Yang Y, Allen E, Ding J, Wang W. Giant axonal neuropathy. *Cell Mol Life Sci*. 2007;64(5):601–609.
6. Dhanoa BS, Cogliati T, Satish AG, Bruford EA, Friedman JS. Update on the Kelch-like (KLHL) gene family. *Hum Genomics*. 2013;7:13.
7. Furukawa M, He YJ, Borchers C, Xiong Y. Targeting of protein ubiquitination by BTB-Cullin 3-Roc1 ubiquitin ligases. *Nat Cell Biol*. 2003;5(11):1001–1007.
8. Bomont P, Koenig M. Intermediate filament aggregation in fibroblasts of giant axonal neuropathy patients is aggravated in non dividing cells and by microtubule destabilization. *Hum Mol Genet*. 2003;12(8):813–822.
9. Boizot A, et al. The instability of the BTB-KELCH protein Gigaxonin causes giant axonal neuropathy and constitutes a new penetrant and specific diagnostic test. *Acta Neuropathol Commun*. 2014;2:47.
10. Lowery J, et al. Abnormal intermediate filament organization alters mitochondrial motility in giant axonal neuropathy fibroblasts. *Mol Biol Cell*. 2016;27(4):608–616.
11. Cleveland DW, Yamanaka K, Bomont P. Gigaxonin controls vimentin organization through a tubulin chaperone-independent pathway. *Hum Mol Genet*. 2009;18(8):1384–1394.
12. Mahammad S, et al. Giant axonal neuropathy-associated gigaxonin mutations impair intermediate filament protein degradation. *J Clin Invest*. 2013;123(5):1964–1975.
13. Israeli E, et al. Intermediate filament aggregates cause mitochondrial dysmotility and increase energy demands in giant axonal neuropathy. *Hum Mol Genet*. 2016;25(11):2143–2157.
14. Chen PH, et al. Glycosylation of KEAP1 links nutrient sensing to redox stress signaling. *EMBO J*. 2017;36(15):2233–2250.
15. Hart GW, Slawson C, Ramirez-Correa G, Lagerlof O. Cross talk between O-GlcNAcylation and phosphorylation: roles in signaling, transcription, and chronic disease. *Annu Rev Biochem*. 2011;80:825–858.
16. Hanover JA, Krause MW, Love DC. The hexosamine signaling pathway: O-GlcNAc cycling in feast or famine. *Biochim Biophys Acta*. 2010;1800(2):80–95.
17. Hart GW. Three decades of research on *O*-GlcNAcylation — a major nutrient sensor that regulates signaling, transcription and cellular metabolism. *Front Endocrinol (Lausanne)*. 2014;5:183.
18. Bond MR, Hanover JA. A little sugar goes a long way: the cell biology of O-GlcNAc. *J Cell Biol*. 2015;208(7):869–880.
19. Hart GW, Housley MP, Slawson C. Cycling of O-linked beta-N-acetylglucosamine on nucleocytoplasmic proteins. *Nature*. 2007;446(7139):1017–1022.
20. Wells L, Vosseller K, Hart GW. Glycosylation of nucleocytoplasmic proteins: signal transduction and O-GlcNAc. *Science*. 2001;291(5512):2376–2378.
21. Love DC, Hanover JA. The hexosamine signaling pathway: deciphering the "O-GlcNAc code." *Sci STKE*. 2005;2005(312):re13.
22. Bond MR, Hanover JA. O-GlcNAc cycling: a link between metabolism and chronic disease. *Annu Rev Nutr*. 2013;33:205–229.
23. Mondoux MA, et al. O-linked-N-acetylglucosamine cycling and insulin signaling are required for the glucose stress response in Caenorhabditis elegans. *Genetics*. 2011;188(2):369–382.
24. Kreppel LK, Hart GW. Regulation of a cytosolic and nuclear O-GlcNAc transferase. Role of the tetratricopeptide repeats. *J Biol Chem*. 1999;274(45):32015–32022.
25. Ruan HB, et al. O-GlcNAc transferase/host cell factor C1 complex regulates gluconeogenesis by modulating PGC-1α stability. *Cell Metab*. 2012;16(2):226–237.
26. Ruan HB, et al. O-GlcNAc transferase enables AgRP neurons to suppress browning of white fat. *Cell*. 2014;159(2):306–317.
27. Taylor RP, Geisler TS, Chambers JH, McClain DA. Up-regulation of O-GlcNAc transferase with glucose deprivation in HepG2 cells is mediated by decreased hexosamine pathway flux. *J Biol Chem*. 2009;284(6):3425–3432.
28. Taylor RP, et al. Glucose deprivation stimulates O-GlcNAc modification of proteins through up-regulation of O-linked N-acetylglucosaminyltransferase. *J Biol Chem*. 2008;283(10):6050–6057.
29. Liu K, Paterson AJ, Chin E, Kudlow JE. Glucose stimulates protein modification by O-linked GlcNAc in pancreatic beta cells: linkage of O-linked GlcNAc to beta cell death. *Proc Natl Acad Sci U S A*. 2000;97(6):2820–2825.
30. Cheung WD, Hart GW. AMP-activated protein kinase and p38 MAPK activate O-GlcNAcylation of neuronal proteins during glucose deprivation. *J Biol Chem*. 2008;283(19):13009–13020.
31. Shafi R, et al. The O-GlcNAc transferase gene resides on the X chromosome and is essential for embryonic stem cell viability and mouse ontogeny. *Proc Natl Acad Sci U S A*. 2000;97(11):5735–5739.
32. Keembiyehetty C, Love DC, Harwood KR, Gavrilova O, Comly ME, Hanover JA. Conditional knockout reveals a requirement for O-linked N-Acetylglucosaminase (O-GlcNAcase) in metabolic homeostasis. *J Biol Chem*. 2015;290(11):7097–7113.
33. Yang YR, et al. O-GlcNAcase is essential for embryonic development and maintenance of genomic stability. *Aging Cell*. 2012;11(3):439–448.
34. Wang P, Hanover JA. Nutrient-driven O-GlcNAc cycling influences autophagic flux and neurodegenerative proteotoxicity. *Autophagy*. 2013;9(4):604–606.
35. Shin SH, Love DC, Hanover JA. Elevated O-GlcNAc-dependent signaling through inducible mOGT expression selectively trig-

gers apoptosis. *Amino Acids*. 2011;40(3):885–893.
36. Lazarus BD, Love DC, Hanover JA. O-GlcNAc cycling: implications for neurodegenerative disorders. *Int J Biochem Cell Biol*. 2009;41(11):2134–2146.
37. Hanover JA, Wang P. O-GlcNAc cycling shows neuroprotective potential in C. elegans models of neurodegenerative disease. *Worm*. 2013;2(4):e27043.
38. Akan I, Olivier-Van Stichelen S, Bond MR, Hanover JA. Nutrient-driven O-GlcNAc in proteostasis and neurodegeneration. *J Neurochem*. 2018;144(1):7–34.
39. Yuzwa SA, et al. Increasing O-GlcNAc slows neurodegeneration and stabilizes tau against aggregation. *Nat Chem Biol*. 2012;8(4):393–399.
40. Vaidyanathan K, Durning S, Wells L. Functional O-GlcNAc modifications: implications in molecular regulation and pathophysiology. *Crit Rev Biochem Mol Biol*. 2014;49(2):140–163.
41. Yuzwa SA, Vocadlo DJ. O-GlcNAc and neurodegeneration: biochemical mechanisms and potential roles in Alzheimer's disease and beyond. *Chem Soc Rev*. 2014;43(19):6839–6858.
42. Zhu Y, Shan X, Yuzwa SA, Vocadlo DJ. The emerging link between O-GlcNAc and Alzheimer disease. *J Biol Chem*. 2014;289(50):34472–34481.
43. Chen PH, Chi JT, Boyce M. KEAP1 has a sweet spot: a new connection between intracellular glycosylation and redox stress signaling in cancer cells. *Mol Cell Oncol*. 2017;4(6):e1361501.
44. Chen PH, Chi JT, Boyce M. Functional crosstalk among oxidative stress and O-GlcNAc signaling pathways. *Glycobiology*. 2018;28(8):556–564.
45. Soomro A, et al. Giant axonal neuropathy alters the structure of keratin intermediate filaments in human hair. *J R Soc Interface*. 2017;14(129):20170123.
46. Treiber-Held S, Budjarjo-Welim H, Reimann D, Richter J, Kretzschmar HA, Hanefeld F. Giant axonal neuropathy: a generalized disorder of intermediate filaments with longitudinal grooves in the hair. *Neuropediatrics*. 1994;25(2):89–93.
47. Johnson-Kerner BL, Roth L, Greene JP, Wichterle H, Sproule DM. Giant axonal neuropathy: an updated perspective on its pathology and pathogenesis. *Muscle Nerve*. 2014;50(4):467–476.
48. Scrivo A, Codogno P, Bomont P. Gigaxonin E3 ligase governs ATG16L1 turnover to control autophagosome production. *Nat Commun*. 2019;10(1):780.
49. Johnson-Kerner BL, Garcia Diaz A, Ekins S, Wichterle H. Kelch Domain of gigaxonin interacts with intermediate filament proteins affected in giant axonal neuropathy. *PLoS ONE*. 2015;10(10):e0140157.
50. Bomont P. Degradation of the intermediate filament family by gigaxonin. *Meth Enzymol*. 2016;569:215–231.
51. Dequen F, Bomont P, Gowing G, Cleveland DW, Julien JP. Modest loss of peripheral axons, muscle atrophy and formation of brain inclusions in mice with targeted deletion of gigaxonin exon 1. *J Neurochem*. 2008;107(1):253–264.
52. Ganay T, Boizot A, Burrer R, Chauvin JP, Bomont P. Sensory-motor deficits and neurofilament disorganization in gigaxonin-null mice. *Mol Neurodegener*. 2011;6:25.
53. Armao D, Bailey RM, Bouldin TW, Kim Y, Gray SJ. Autonomic nervous system involvement in the giant axonal neuropathy (GAN) KO mouse: implications for human disease. *Clin Auton Res*. 2016;26(4):307–313.
54. Sanjana NE, Shalem O, Zhang F. Improved vectors and genome-wide libraries for CRISPR screening. *Nat Methods*. 2014;11(8):783–784.
55. Tarbet HJ, et al. Site-specific glycosylation regulates the form and function of the intermediate filament cytoskeleton. *Elife*. 2018;7:e31807.
56. Shaw G, Morse S, Ararat M, Graham FL. Preferential transformation of human neuronal cells by human adenoviruses and the origin of HEK 293 cells. *FASEB J*. 2002;16(8):869–871.
57. Allen E, et al. Gigaxonin-controlled degradation of MAP1B light chain is critical to neuronal survival. *Nature*. 2005;438(7065):224–228.
58. Wang W, et al. Gigaxonin interacts with tubulin folding cofactor B and controls its degradation through the ubiquitin-proteasome pathway. *Curr Biol*. 2005;15(22):2050–2055.
59. Slawson C, Zachara NE, Vosseller K, Cheung WD, Lane MD, Hart GW. Perturbations in O-linked beta-N-acetylglucosamine protein modification cause severe defects in mitotic progression and cytokinesis. *J Biol Chem*. 2005;280(38):32944–32956.
60. Szklarczyk D, et al. The STRING database in 2017: quality-controlled protein-protein association networks, made broadly accessible. *Nucleic Acids Res*. 2017;45(D1):D362–D368.
61. Zhang DD, Lo SC, Sun Z, Habib GM, Lieberman MW, Hannink M. Ubiquitination of Keap1, a BTB-Kelch substrate adaptor protein for Cul3, targets Keap1 for degradation by a proteasome-independent pathway. *J Biol Chem*. 2005;280(34):30091–30099.
62. Ridge KM, et al. Methods for determining the cellular functions of vimentin intermediate filaments. *Meth Enzymol*. 2016;568:389–426.
63. Bond MR, Hanover JA. O-GlcNAc cycling: a link between metabolism and chronic disease. *Annu Rev Nutr*. 2013;33:205–229.
64. Zachara NE, Hart GW. O-GlcNAc a sensor of cellular state: the role of nucleocytoplasmic glycosylation in modulating cellular function in response to nutrition and stress. *Biochim Biophys Acta*. 2004;1673(1–2):13–28.
65. Slawson C, Lakshmanan T, Knapp S, Hart GW. A mitotic GlcNAcylation/phosphorylation signaling complex alters the post-translational state of the cytoskeletal protein vimentin. *Mol Biol Cell*. 2008;19(10):4130–4140.
66. Chou CF, Omary MB. Mitotic arrest-associated enhancement of O-linked glycosylation and phosphorylation of human keratins 8 and 18. *J Biol Chem*. 1993;268(6):4465–4472.
67. Haltiwanger RS, Philipsberg GA. Mitotic arrest with nocodazole induces selective changes in the level of O-linked N-acetylglucosamine and accumulation of incompletely processed N-glycans on proteins from HT29 cells. *J Biol Chem*. 1997;272(13):8752–8758.
68. Tang X, et al. Comprehensive profiling of amino acid response uncovers unique methionine-deprived response dependent on intact creatine biosynthesis. *PLoS Genet*. 2015;11(4):e1005158.
69. Johnson-Kerner BL, et al. Intermediate filament protein accumulation in motor neurons derived from giant axonal neuropathy iPSCs rescued by restoration of gigaxonin. *Hum Mol Genet*. 2015;24(5):1420–1431.
70. Arribat Y, et al. Sonic Hedgehog repression underlies gigaxonin mutation–induced motor deficits in giant axonal neuropathy.

J Clin Invest. 2019;129(12):5312–53268.
71. Cerami E, et al. The cBio cancer genomics portal: an open platform for exploring multidimensional cancer genomics data. *Cancer Discov*. 2012;2(5):401–404.
72. Gao J, et al. Integrative analysis of complex cancer genomics and clinical profiles using the cBioPortal. *Sci Signal*. 2013;6(269):pl1.
73. Richardson AM, et al. Vimentin is required for lung adenocarcinoma metastasis via heterotypic tumor cell-cancer-associated fibroblast interactions during collective invasion. *Clin Cancer Res*. 2018;24(2):420–432.
74. Kidd ME, Shumaker DK, Ridge KM. The role of vimentin intermediate filaments in the progression of lung cancer. *Am J Respir Cell Mol Biol*. 2014;50(1):1–6.
75. Kang JJ, Liu IY, Wang MB, Srivatsan ES. A review of gigaxonin mutations in giant axonal neuropathy (GAN) and cancer. *Hum Genet*. 2016;135(7):675–684.
76. Bailey RM, Armao D, Nagabhushan Kalburgi S, Gray SJ. Development of intrathecal AAV9 gene therapy for giant axonal neuropathy. *Mol Ther Methods Clin Dev*. 2018;9:160–171.
77. Mussche S, et al. Restoration of cytoskeleton homeostasis after gigaxonin gene transfer for giant axonal neuropathy. *Hum Gene Ther*. 2013;24(2):209–219.
78. Deutsch EW, et al. The ProteomeXchange consortium in 2017: supporting the cultural change in proteomics public data deposition. *Nucleic Acids Res*. 2017;45(D1):D1100–D1106.
79. Perez-Riverol Y, et al. The PRIDE database and related tools and resources in 2019: improving support for quantification data. *Nucleic Acids Res*. 2019;47(D1):D442–D450.
80. Sanjana NE, Shalem O, Zhang F. Improved vectors and genome-wide libraries for CRISPR screening. *Nat Methods*. 2014;11(8):783–784.